Great Britain Journals Press

Print ISSN: 2631-8474
Online ISSN: 2631-8482
DOI: 10.17406/LJER

London Journal of Engineering Research

Volume 26 | Issue 1 | Compilation 1.0

COMPILED IN UNITED KINGDOM

MULTILINGUAL

IN THIS ISSUE

GREAT BRITAIN JOURNALS PRESS

London Journal of Engineering Research

General Catalogue

Volume 26 Issue 1 2026

EDITION

Digital Journal

Released digital issue assembled for the public journal archive.

REGISTER

LJER / 26.1

PUBLICATION DOSSIER

LJER - Section

Engineering research register for systems, fabrication, materials, and industrial practice.

PUBLISHER

Great Britain Journals Press
United States

ISSUE RECORD

LJER Volume 26 Issue 1

CIRCULATION BASIS

This compiled issue file is distributed for archive, cataloguing, review, and citation continuity. Individual article records retain their own article-level rights and metadata.

Oversight and Review Route

Editorial review in LJER prioritizes method traceability, dimensional clarity, standards references, and realistic statements about deployment, maintenance, and operating conditions.

PRIMARY ROUTE

Editorial Office, Great Britain Journals Press
journalspress.com

Issue Prospectus

This issue register in London Journal of Engineering Research is organized for apparatus-driven studies, fabrication records, design reasoning, and field-tested engineering analysis.

Contributors are expected to keep units, tolerances, schematics, and performance claims explicit so that the issue file reads like an auditable engineering record rather than a promotional digest.

Issue Register

Great Britain Journals Press

London Journal of Engineering Research
General Section

RESEARCH FINGERPRINT

IDENTIFIER
LJER-227654

PEER REVIEW
Double Blind

SIMILARITY CHECK
Perplexity AI and iThenticate

ACCESS
Open Access

LANGUAGE
English

PRINT ISSN
2631-8474

ONLINE ISSN
2631-8482

EDITION

ABBREVIATION
LJER

VOLUME
26

ISSUE
1

YEAR
2026

KEY DATES

RECEIVED
2026-05-04

ACCEPTED
2026-05-11

ONLINE PUBLISHED
2026-06-03

PUBLISHED
2026-06-26

CATALOGING

CROSSMARK DOI
10.34257/LJER227654UK

UDC CLASS
624.131.3

IEEE CLASS
Geotechnical engineering

ARXIV CLASS
physics.geo-ph

LCC CLASS
QE598.2

Article Record

Study on Changes in Groundwater Level Decline Rates on Slopes

CORRESPONDENCE

AUTHORS & AFFILIATIONS

Ken-Ling Lin ¶*

Wei Fang

Min-Xi Xie

Chen-Kan Liao

Ying-Han Chen

¶ Computer Science, Rajiv Gandhi Bhopal, India

ABSTRACT

This study used a Sanlien VW-dot data logger and vibrating-wire electronic piezometers to record continuous groundwater level data from monitoring wells at one-hour intervals. We attempted to stratify the subsurface by analyzing changes in groundwater level decline rates. The observations indicate that the decline rate (slope) generally decreases with depth, which may reflect lower fracture density and connectivity in rock masses or increased compactness of deeper soil layers. The stratification process selected segments with regular decline rates and grouped segments with similar slopes into the same layer. Better layer boundaries were calibrated using multiple line segments with different slope values and depth ranges. Regular decline slopes usually appear several hours after rainfall and are related to local geology, hydrology, and lithology. Because fracture saturation and seepage-equilibrium times differ, the onset time of regular slopes also differs. During stratification, obvious interference from subsequent rainfall should be avoided. In addition, some boundaries still show identifiable differences in variability, so sublayers can be further defined; the causes of these differences are discussed in the paper. Overall, decline-rate stratification generally decreases with depth and is related to weathering, effective fracture ratio, or RQD from shallow to deep strata. Engineering factors, such as horizontal drainage from catch wells and the compaction quality of backfilled trench areas after underground pipeline works, can also affect layer thickness.

Index Terms: Groundwater Level • Decline Rate • Slope Monitoring • Subsurface Stratification • Piezometer • Hydraulic Conductivity

FUNDING
No external funding was declared for this work.

CONFLICTS
The authors declare no conflict of interest.

AI USAGE
No generative AI was used for analysis or results.

HOW TO CITE
Lin et al. (2026). Study on Changes in Groundwater Level Decline Rates on Slopes. London Journal of Engineering Research, 26(1), 1-6. DOI: 10.34257/LJER227654UK

ACCESS ONLINE

METADATA CONTINUATION

AUTHOR CONTACT QR LEDGER

Ken-Ling Lin¶*

ARCHIVAL RECORD

LJER · Vol 26 · Issue 1 · 2026

Article ID LJER-227654 · DOI 10.34257/LJER227654UK

Print ISSN 2631-8474 · Online ISSN 2631-8482

CROSSREF DOI 10.34257/LJER227654UK

RESEARCH ARTICLE

Study on Changes in Groundwater Level Decline Rates on Slopes

Ken-Ling Lin[¶*], Wei Fang[¶], Min-Xi Xie[¶], Chen-Kan Liao[¶], and Ying-Han Chen[¶]

AFFILIATIONS

[¶] Computer Science, Rajiv Gandhi Bhopal, India

Abstract

This study used a Sanlien VW-dot data logger and vibrating-wire electronic piezometers to record continuous groundwater level data from monitoring wells at one-hour intervals. We attempted to stratify the subsurface by analyzing changes in groundwater level decline rates. The observations indicate that the decline rate (slope) generally decreases with depth, which may reflect lower fracture density and connectivity in rock masses or increased compactness of deeper soil layers. The stratification process selected segments with regular decline rates and grouped segments with similar slopes into the same layer. Better layer boundaries were calibrated using multiple line segments with different slope values and depth ranges. Regular decline slopes usually appear several hours after rainfall and are related to local geology, hydrology, and lithology. Because fracture saturation and seepage-equilibrium times differ, the onset time of regular slopes also differs. During stratification, obvious interference from subsequent rainfall should be avoided. In addition, some boundaries still show identifiable differences in variability, so sublayers can be further defined; the causes of these differences are discussed in the paper. Overall, decline-rate stratification generally decreases with depth and is related to weathering, effective fracture ratio, or RQD from shallow to deep strata. Engineering factors, such as horizontal drainage from catch wells and the compaction quality of backfilled trench areas after underground pipeline works, can also affect layer thickness.

Keywords: *Groundwater Level, Decline Rate, Slope Monitoring, Subsurface Stratification, Piezometer, Hydraulic Conductivity*

Correspondence: Ken-Ling Lin

1 Background

The study site is a slope in Wenshan District, Taipei (WS-066). Before development, the area was a concave valley-like terrain and a dip slope composed of interbedded sandstone and shale of the Taliao Formation. Geological profiles show that, after backfilling the original valley topography, the soil layer reached a maximum thickness of about 15 m.

Since 2012, groundwater monitoring had shown anomalies. Toe drainage holes were first added at the slope toe. Groundwater levels decreased slightly but did not reach the expected effect. Therefore, slope anchor reinforcement and catch-well construction were carried out from May 2014 to January 2015. After catch-well installation, nearby monitoring wells showed clear dewatering effects, but groundwater levels at mid-slope wells WS-002-S01 and WS-002-S05 remained consistently high.

WS-002-S01 and WS-002-S05 were damaged during pressurized pipeline maintenance in April 2016 and could not be immediately reset. On October 5, 2016, the Wanfang Fire Department reported abnormal yellow muddy flow on the slope. Field inspectors traced the flow source and confirmed that it was caused by rupture and water outflow from a pressurized pipeline. On the same day, the EOW3 groundwater record also showed an abnormal change. Comparison of several days of rain gauge data (hourly cumulative rainfall) and groundwater level observations before the rupture highlights that EOW3, located approximately 55 m downhill from the rupture, experienced significant anomalous rises independent of rainfall. This high-signal event serves as an excellent real-world ”stress test” demonstrating the sensitivity of the monitoring system to pipeline leakages. After pipeline replacement and reinstallation of WS-002-S01 and WS-002-S05, the long-term groundwater level clearly dropped to GL-4.0 to GL-12.0 m below ground surface.

WS-001-S01 (later WS-002-S01) and WS-002-S05 are manual inclinometer boreholes also used for water-level observations. In June 2019, WS-002-S05 was equipped with an electronic water-level gauge with one record per hour, and the electronic monitoring ID was changed to EOW2. While recording at one-hour intervals is standard for long-term monitoring, the rapid, transient rises of Stage I (occurring within an hour) may exhibit aliasing when captured at this frequency. However, because the primary focus of this study is the stable decline rates during Stages II and III, this discrete hourly sampling rate remains appropriate for the analysis.

As shown in Fig. 1, the monitoring setup is organized into three columns. The first column shows the rain gauge readings (daily rainfall in mm, recorded hourly). The second column shows the manual observation data for WS-002-S01 and WS-002-S05 (measured monthly). The third column shows the electronic observation data for WS-066-EOW3 (recorded hourly). The slope observation wells are arranged sequentially from highest to lowest elevation: WS-002-S05 → WS-002-S01 → WS-066-EOW3. In the second column, manual observation

data is missing during Phase III due to borehole and pipeline damage; data resumes in Phase IV after the boreholes were re-established near the original locations. A clear difference in groundwater trends is observed between the early phases (Phases I and II, characterized by pressurized pipeline leakage) and the later phase (Phase IV, following pipeline repair and showing no obvious leakage). In the third column, WS-066-EOW3 shows the attenuation of pipeline leakage effects and a long-term downward trend in the groundwater level following the construction of two nearby sump wells (Boreholes 1 and 2, which are 5 m in diameter, 10 m deep, and equipped with horizontal drainage holes at approximately 7.8 m depth).

For EOW3, located near the catch well, the groundwater decline-rate parameter K' changed significantly before and after catch-well installation. In engineering practice, changes in groundwater decline rate can be used as a reference indicator for checking horizontal-drain dewatering performance and for analyzing slope seepage behavior.

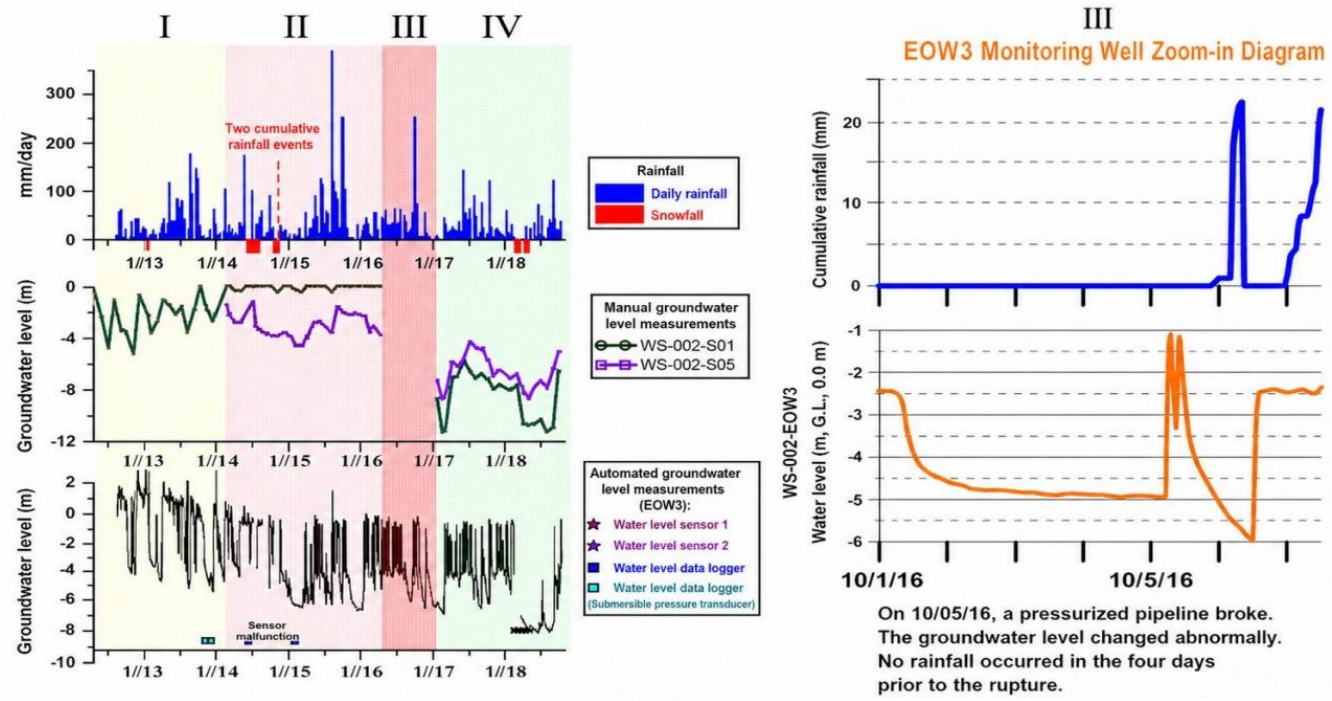

Figure 1. Groundwater observations at the slope from 2012 to 2018 (Stages I-IV), redrawn from Wang et al. [1] and Gao et al. [2].

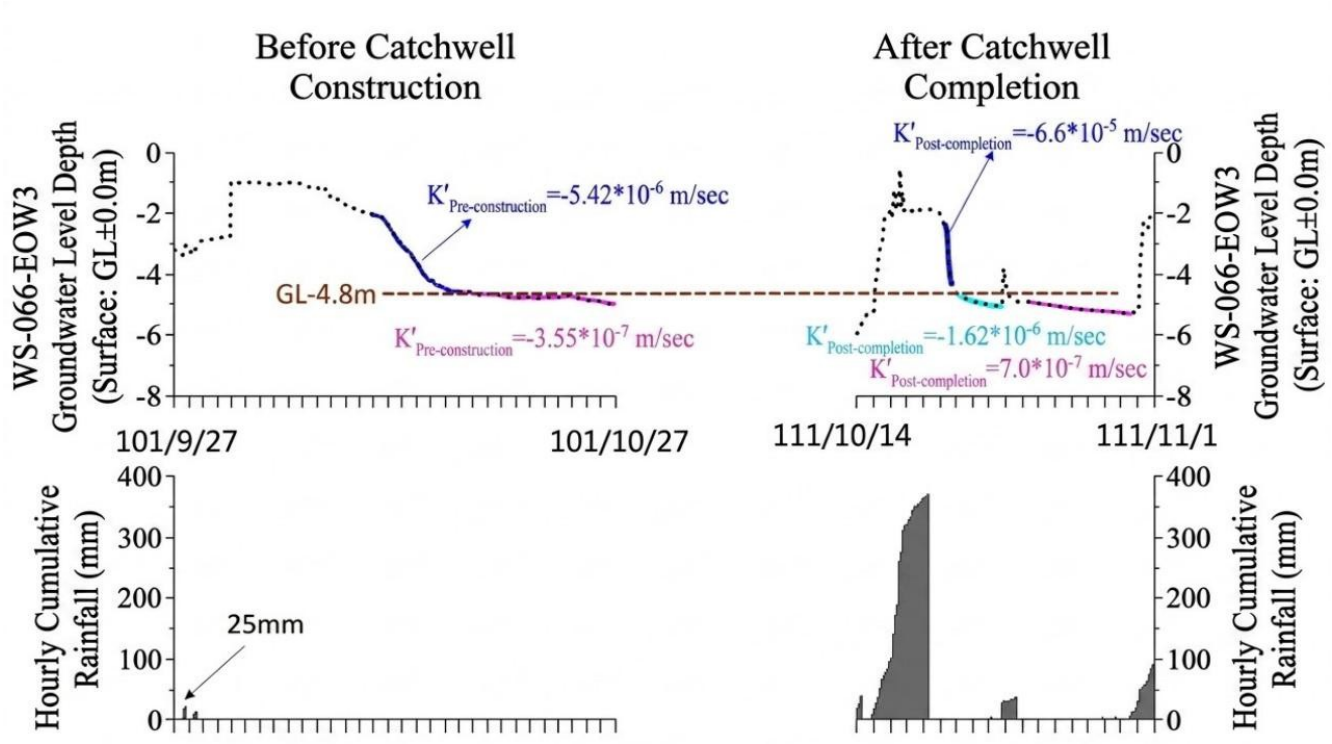

Figure 2. Comparison of EOW3 groundwater decline rates before and after catch-well completion.

2 Method for Stratifying Groundwater Decline Rates

To explain the stratification approach used at WS-066, we first use another slope in Wenshan District, WS-094, as an example by comparing rainfall and groundwater hydrographs. WS-094 is Nankang Formation sandstone with weathered debris at the surface. Stage I is a rising stage in which groundwater rose sharply from about GL-7.0 m to GL-3.0 m within about one hour. Stage II is a decline stage from about GL-3.85 m to GL-5.5 m within about 12 hours, with a decline rate of -4.2×10^{-5} m/s. Stage III shows a slower decline from around GL-5.5 m over about 18 hours, with a decline rate of -4.48×10^{-6} m/s.

During Stage I, rainfall or surface runoff quickly infiltrated underground fractures and caused rapid water rise. This high-transient stage is not suitable for stratification. The stagnation period between Stages I and II is also not suitable. Stages II and III, which show regular decline trends, can be used to distinguish different stratified rates.

The selection of these regular decline segments is evaluated on a case-by-case basis. Because decline thresholds vary across different locations, and there is no universal threshold that applies equally to soil and rock layers, a qualitative check is supplemented by a consistency review of the decline rate over several hours. To ensure a stable seepage state and exclude transient noise, short-duration downpours occurring after long dry spells must be excluded; under such conditions, water drains rapidly through unsaturated fissures, resulting in temporarily faster and non-representative decline rates. Therefore, the strata must be subjected to rainfall for a sufficiently long period to establish a steady-state or fully saturated seepage regime before decline-rate stratification can be reliably applied.

Using this regular-decline concept, multiple single-line segments with similar rates are classified into the same layer, and the layer boundaries are calibrated for best fit. This is the groundwater decline-rate stratification method. Although current results still cannot directly quantify environmental geological sensitivity, they are related to formation permeability. In future work, additional indicators may be integrated, such as rising-rate versus declining-rate relationships, slope gradient, and other statistical indices.

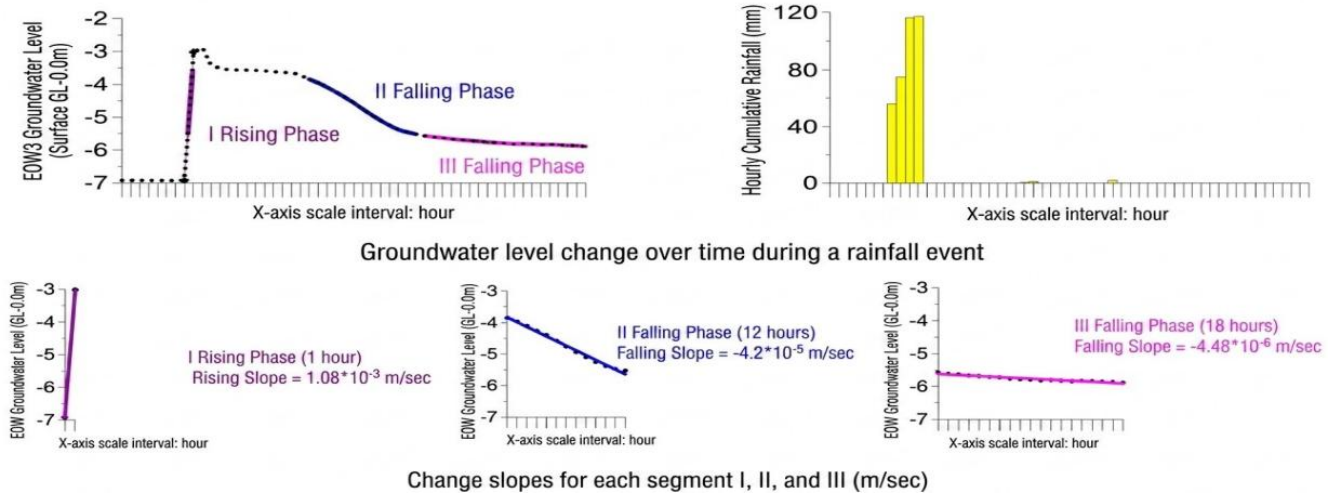

Figure 3. Reference for selecting groundwater decline-rate segments (slope): WS-094 slope.

For WS-066-EOW4, line segments with regular decline rates were selected as stratification references. The selected segments focus on the second layer, decline rates of about $(-1.07$ to $-2.89) \times 10^{-6}$ m/s. The candidate segments above and below the reference line were compared to refine the boundary between the second and third layers. At present, the boundary between those layers is tentatively set at GL-4.8 m.

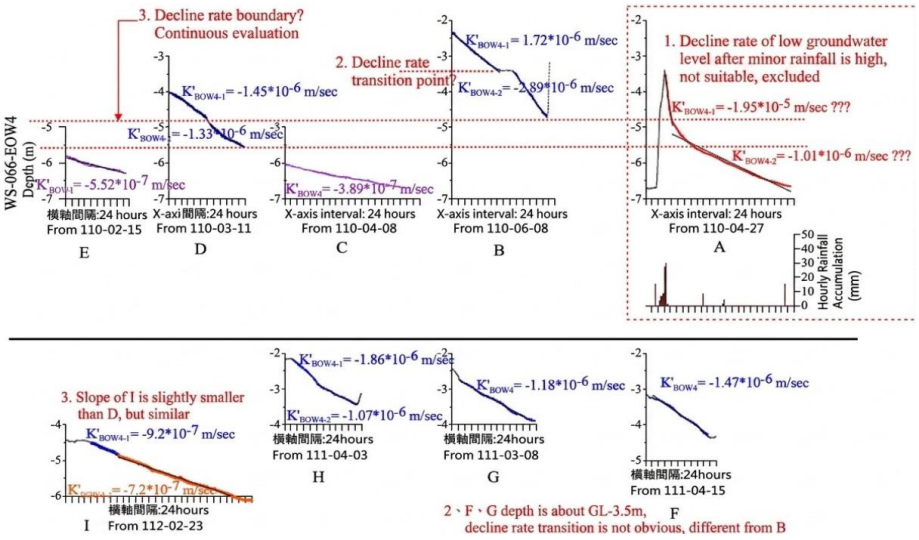

Figure 4. Reference for selecting groundwater decline-rate segments (slope): WS-066 slope.

3 Stratified Profiles and Discussion of Groundwater Decline Rates

3.1 Stratification of Different Groundwater Decline Rates

At this slope, three electronic groundwater monitoring wells are arranged from higher to lower elevation: EOW2 (borehole depth 30 m), EOW4 (15.5 m), and EOW3 (30 m). Their stratifications are summarized below, and the stratified profile is shown in Fig. 5.

EOW2: According to borehole logs, the interval from the surface to about 7.5 m is soil with gravel; 7.5–10 m is weathered sandstone; and 10–30 m is interbedded sandstone and shale. Given the potential for confined-water influence, the geological anisotropy of these interbedded sandstone and shale layers could introduce minor biases in the decline rate calculation compared to the more homogenous overlying soil layers. However, historical monitoring suggests that this influence is relatively small. During the Hualien earthquake on January 3, 2022, where the intensity in Taipei City reached level 4, the hourly groundwater level record (captured approximately 14 minutes post-earthquake) showed a total rise of only 0.73 cm (comprising 0.47 cm and 0.26 cm increases in the two subsequent hourly records), which then gradually decreased over time. Furthermore, comparison of rainfall and groundwater level observations shows a consistent correlation, and the decline-rate stratification boundaries align well with the recorded depths of soil displacement changes. Nonetheless, the anisotropy of interbedded formations remains a limitation, and monitoring locations with significant confined-water influence should generally be avoided unless calibration methods are available. Although the measured groundwater level may be slightly higher than the actual free-water level, the rise-fall pattern is still consistent with rainfall, and the decline-rate changes remain systematically interpretable; therefore EOW2 is included in the stratified profile.

EOW2 stratification: from ground surface downward, three primary layers are identified. Layer 1 K_1' extends from GL-0.0 to GL-2.6 m and is subdivided at GL-1.3 m into $K_1'a_{\mathrm{EOW2}}$ and $K_1'b_{\mathrm{EOW2}}$. Layer 2 K_2' is subdivided at GL-4.7 m into $K_2'a_{\mathrm{EOW2}}$ and $K_2'b_{\mathrm{EOW2}}$. Layer 3 $K'_{3_{\mathrm{EOW2}}}$ lies deeper than GL-5.8 m.

EOW4: Geological profile interpretation suggests that the 15 m depth is mainly within soil. EOW4 stratification has three primary layers from surface downward: Layer 1 from GL-0.0 to GL-2.1 m, Layer 2 from GL-2.1 to GL-4.8 m, and Layer 3 below GL-4.8 m. The GL-4.8 m boundary between Layers 2 and 3 is tentative and still under evaluation.

EOW3: EOW3 stratification has two primary layers from surface downward. Layer 1 is GL-0.0 to GL-4.8 m and can be subdivided at GL-2.2 m into $K_1'a_{\mathrm{EOW3}}$ and $K_1'b_{\mathrm{EOW3}}$. Layer 2 is approximately GL-4.8 to GL-5.1 m.

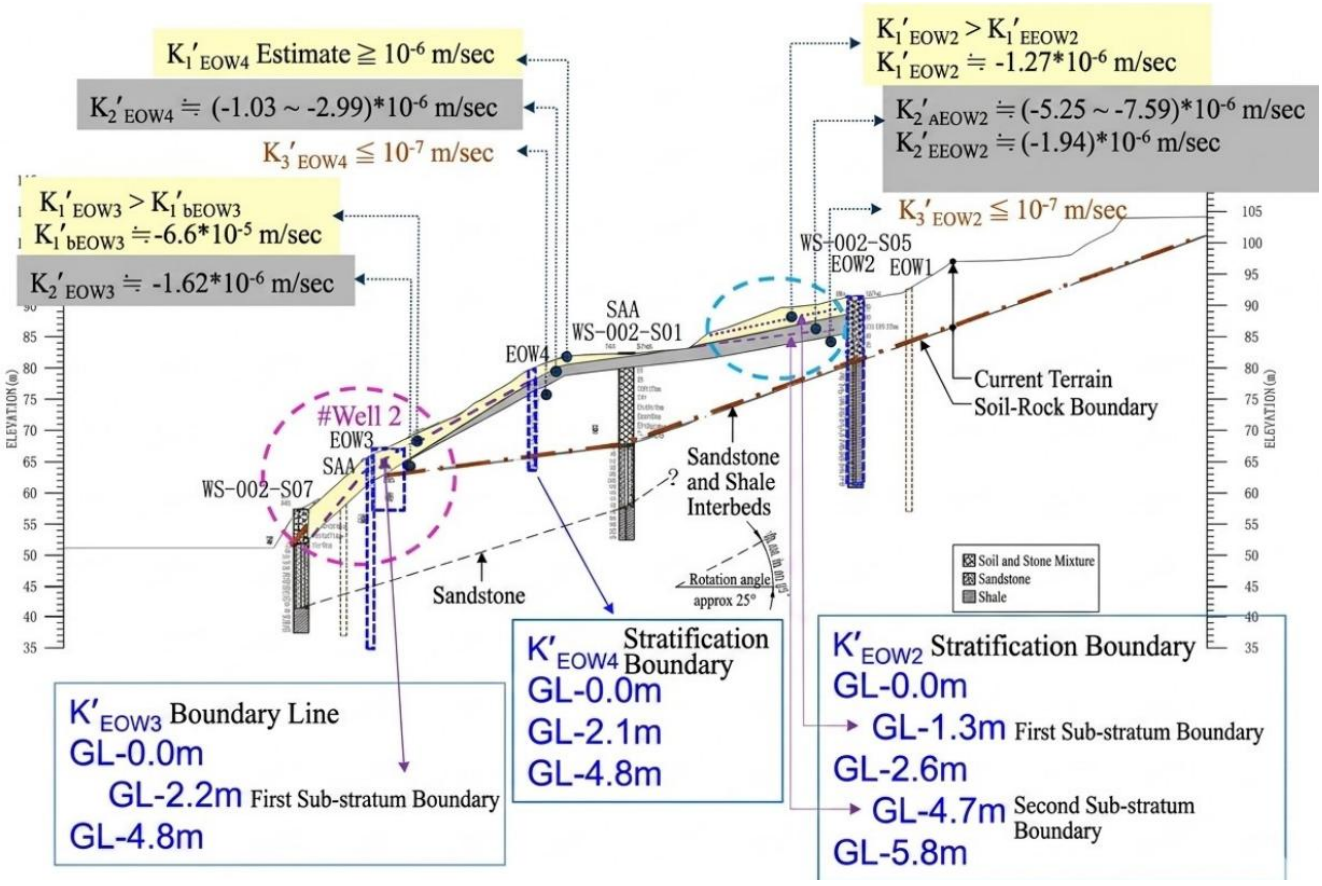

Figure 5. Stratified profile of different groundwater decline rates at WS-066.

3.2 Discussion of Causes of Stratification Differences Among Wells

The total stratified thickness of EOW2 is slightly greater than that of EOW4. A likely reason is that the slope area below EOW2 contains buried pressurized pipelines. Pipeline maintenance or replacement requires excavation and surface restoration, and the restored backfill zone, visually about 3–4 m deep, may not be fully compacted, resulting in a slightly greater stratified thickness range.

EOW4 has only about two layers within GL-0.0 to GL-4.8 m, unlike EOW2 and EOW3, which can be subdivided further. Since no additional human-induced terrain modification occurred near this observation

Table 1. Stratification of groundwater decline rates at EOW2

Layer	Depth Range (m)	Decline Rate (m/s)
Layer 1 $K'_1 a_{\mathrm{EOW2}}$	GL-0.0 to GL-1.3	$K'_1 a_{\mathrm{EOW2}} > K'_1 b_{\mathrm{EOW2}}$
Layer 1 $K'_1 b_{\mathrm{EOW2}}$	GL-1.3 to GL-2.6	-1.27×10^{-5}
Layer 2 $K'_2 a_{\mathrm{EOW2}}$	GL-2.6 to GL-4.7	$(-5.25 \text{ to } -7.59) \times 10^{-6}$
Layer 2 $K'_2 b_{\mathrm{EOW2}}$	GL-4.7 to GL-5.8	-1.94×10^{-6}
Layer 3 $K'_{3_{\mathrm{EOW2}}}$	Below GL-5.8	$\sim 10^{-7}$

Table 2. Stratification of groundwater decline rates at EOW4

Layer	Depth Range (m)	Decline Rate (m/s)
Layer 1 $K'_{1_{\mathrm{EOW4}}}$	GL-0.0 to GL-2.1	Estimated $> 10^{-6}$
Layer 2 $K'_{2_{\mathrm{EOW4}}}$	GL-2.1 to GL-4.8	$(-1.07 \text{ to } -2.89) \times 10^{-6}$
Layer 3 $K'_{3_{\mathrm{EOW4}}}$	Below GL-4.8	Lower than Layer 2[a]

[a]*Boundary between Layers 2 and 3 is tentative and under evaluation.*

Table 3. Stratification of groundwater decline rates at EOW3

Layer	Depth Range (m)	Decline Rate (m/s)
Layer 1 $K'_1 a_{\mathrm{EOW3}}$	GL-0.0 to GL-2.2	$> K'_1 b_{\mathrm{EOW3}}$
Layer 1 $K'_1 b_{\mathrm{EOW3}}$	GL-2.2 to GL-4.8	-6.6×10^{-5}
Layer 2 $K'_2 a_{\mathrm{EOW3}}$	GL-4.8 to GL-5.1	-1.62×10^{-6}

well after development, EOW4 is likely representative of decline-rate stratification in the project backfill area.

Regarding the future application of decline-rate stratification in environmental geological sensitivity analysis, several statistical parameters show promise for quantifying sensitivity based on the current observations. These include: (1) the standard deviation of decline rates within a single stratified layer, which represents layer homogeneity and hydrological anisotropy; (2) the ratio of rising-rate to declining-rate, reflecting fracture connectivity and saturation speed; (3) the coefficient of determination (R^2) from linear regressions of decline segments, indicating the regularity and predictability of the drainage process; and (4) the elevation-dependent variation of decline rates across the slope (e.g., comparing EOW2, EOW4, and EOW3) to characterize spatial heterogeneity. Currently, decline rates must be analyzed on a case-by-case basis for individual slopes, but compiling these statistical indicators across multiple sites could eventually yield standardized sensitivity thresholds.

EOW3 is an existing on-site well with a depth of 30 m and no available drilling log. Nearby drilling records and profiles suggest very shallow weathered soil and sandstone. Since August 2012, hourly electronic records have shown groundwater rise-fall behavior consistent with rainfall, and no abrupt earthquake-induced rises were identified. EOW3 can therefore be treated as a free-water observation well. Before catch-well construction, even small rainfall could rapidly raise groundwater to around GL-1.0 m below the surface, followed by very slow decline. The large difference in decline rates before and after completion of the catch well indicates that EOW3 decline rates are significantly affected by dewatering from the horizontal drains installed with the catch well. Groundwater decline rate can therefore be used as a reference indicator for catch-well performance checks and later maintenance. Proposing specific dewatering maintenance thresholds would significantly enhance the engineering utility of these observations. Based on the long-term observation data of WS-066-EOW3, a groundwater depth of GL-2.0 m and a groundwater decline rate of -6.6×10^{-5} m/s serve as critical baseline indicators. Under typhoon or heavy rain conditions, the groundwater level should drop immediately after the rainfall decreases or stops. A lack of significant drop indicates drainage hole clogging or active pipeline leakage, which can be confirmed by comparing the response to the rain gauge. Conversely, during dry periods with no rainfall, any small anomalous water-level increase is easily diagnosed as a pressurized pipeline leak. These proposed thresholds and diagnostic actions are summarized in Table 4. Because these indicators depend directly on the well's distance from the catch well and local geological strata, they are case-specific and cannot be generalized without local calibration.

Table 4. Proposed Maintenance and Inspection Thresholds for Catch-Well EOW3

Observation Indicator	Threshold / Range	Implied Condition / Diagnosis	Recommended Action
Post-rainfall decline rate K'	$\geq -6.6 \times 10^{-5}$ m/s (i.e., slower rate)	Possible drain clogging or pipeline leakage	Perform rain comparison; inspect/clean drains
Dry-season groundwater level	Anomalous rise or stabilization above GL-2.0 m	Active pressurized pipeline leakage	Conduct pressure testing and leak tracing
Normal decline rate K'	Consistent with Table 3 values	Normal drainage and seepage behavior	Routine periodic maintenance

Note: These thresholds are case-specific to the geology and catch-well configuration of WS-066-EOW3 and cannot be generalized without local calibration.

4 Conclusions

1. Stratified decline rates generally decrease with depth. This trend is likely related to hydrology and geological weathering. Layer thickness may also be influenced by slope gradient, geomaterial properties, bedding attitude, hydrology, and local engineering conditions.

2. At EOW2, the total thickness of Layers 1 and 2 is slightly greater than at EOW4. A likely reason is that the buried pressurized pipeline area below EOW2 underwent excavation and surface restoration during maintenance or replacement. The restored backfill zone, visually about 3–4 m deep, may have been disturbed or incompletely compacted, causing slightly greater layer thickness and faster decline rates. At EOW4, where no subsequent terrain modification occurred after development, groundwater decline rates below GL-2.1 m are relatively low.

3. At EOW3, decline rates can be used to evaluate horizontal-drain dewatering effectiveness before and after catch-well construction. They can also support long-term performance checks after years of operation and serve as an important reference for catch-well maintenance management.

REFERENCES

[1] Wang, R.-Q., Chen, J.-F., and Liao, C.-K. (2021). Safety management and disaster prevention for dip-slope patrol and monitoring in Taipei City. *Geology*, 40(3-4), 65-69. (in Chinese)

[2] Gao, Q.-Z., Lin, K.-L., Lu, W.-X., Lin, S.-Y., Xie, M.-X., and Liao, C.-K. (2021). Groundwater monitoring for a dip-slope case in Taipei City. *Geotechnical Engineer*, 23, 22-35. (in Chinese)

Great Britain Journals Press

London Journal of Engineering Research
General Section

RESEARCH FINGERPRINT

IDENTIFIER
LJER-227083

PEER REVIEW
Double Blind

SIMILARITY CHECK
Perplexity AI and iThenticate

ACCESS
Open Access

LANGUAGE
English

PRINT ISSN
2631-8474

ONLINE ISSN
2631-8482

EDITION

ABBREVIATION
LJER

VOLUME
26

ISSUE
1

YEAR
2026

KEY DATES

RECEIVED
2026-04-15

ACCEPTED
2026-04-27

ONLINE PUBLISHED
2026-05-21

PUBLISHED
2026-06-26

CATALOGING

CROSSMARK DOI
10.34257/LJER227083UK

DDC CLASS
658.872, 338.642, 380.1

Article Record

Digital Marketing and Market Competitiveness of MSME, Cottage, and Rural Industry Products in Gujarat

CORRESPONDENCE

AUTHORS & AFFILIATIONS

Vijay Virambhai Chaudhari ¶*

Sr industries inspector

¶ Industries Department Gujarat India

ABSTRACT

Digital marketing is increasingly shaping the competitiveness of Micro, Small and Medium Enterprises (MSMEs), cottage industries, and rural product enterprises by improving visibility, reducing intermediary dependence, widening customer reach, and enabling product differentiation. This paper develops an IEEE-style conceptual and policy-grounded study focused on Gujarat, a state with strong MSME depth and a distinctive ecosystem of handloom, handicraft, khadi, agro-processing, and village products. The paper combines official policy context, current national MSME dashboard statistics, digital commerce inclusion logic, and a field-oriented research design to examine how social media, messaging commerce, online catalogues, and e-marketplaces influence competitiveness outcomes. The proposed model links digital marketing adoption with market access, customer trust, conversion, sales growth, and margin improvement, while recognizing moderating constraints such as digital literacy, logistics, packaging, language, and payment confidence. The paper concludes that digital marketing should be treated not merely as a promotion channel but as a competitiveness infrastructure for Gujarat's MSME and rural product economy.

Index Terms: digital marketing • MSME • cottage industries • rural industries • Gujarat • competitiveness • artisans • e-commerce • branding • ONDC

FUNDING
No external funding was declared for this work.

CONFLICTS
The authors declare no conflict of interest.

AI USAGE
No generative AI was used for analysis or results.

HOW TO CITE
Virambhai Chaudhari (2026). Digital Marketing and Market Competitiveness of MSME, Cottage, and Rural Industry Products in Gujarat. London Journal of Engineering Research, 26(1), 7-10. DOI: 10.34257/LJER227083UK

ACCESS ONLINE

METADATA CONTINUATION

AUTHOR CONTACT QR LEDGER

Vijay Virambhai Chaudhari¶[1]*

ARCHIVAL RECORD

LJER · Vol 26 · Issue 1 · 2026

Article ID LJER-227083 · DOI 10.34257/LJER227083UK

Print ISSN 2631-8474 · Online ISSN 2631-8482

CROSSREF DOI 10.34257/LJER227083UK

RESEARCH ARTICLE

Digital Marketing and Market Competitiveness of MSME, Cottage, and Rural Industry Products in Gujarat

Vijay Virambhai Chaudhari[¶ǁ*]

QUALIFICATIONS / ROLES

ǁ Sr industries inspector

AFFILIATIONS

¶ Industries Department Gujarat India

Abstract

Digital marketing is increasingly shaping the competitiveness of Micro, Small and Medium Enterprises (MSMEs), cottage industries, and rural product enterprises by improving visibility, reducing intermediary dependence, widening customer reach, and enabling product differentiation. This paper develops an IEEE-style conceptual and policy-grounded study focused on Gujarat, a state with strong MSME depth and a distinctive ecosystem of handloom, handicraft, khadi, agro-processing, and village products. The paper combines official policy context, current national MSME dashboard statistics, digital commerce inclusion logic, and a field-oriented research design to examine how social media, messaging commerce, online catalogues, and e-marketplaces influence competitiveness outcomes. The proposed model links digital marketing adoption with market access, customer trust, conversion, sales growth, and margin improvement, while recognizing moderating constraints such as digital literacy, logistics, packaging, language, and payment confidence. The paper concludes that digital marketing should be treated not merely as a promotion channel but as a competitiveness infrastructure for Gujarat's MSME and rural product economy.

Keywords: *digital marketing, MSME, cottage industries, rural industries, Gujarat, competitiveness, artisans, e-commerce, branding, ONDC*

Correspondence: Vijay Virambhai Chaudhari

1 Introduction

India's MSME ecosystem remains central to output, exports, employment generation, and inclusive industrial growth. The Ministry of MSME states in its Annual Report 2024-25 that the sector contributes around 30% of India's GDP and over 45% of India's exports, underscoring the continued relevance of competitiveness-enhancing interventions for small enterprises. For Gujarat, the issue is particularly important because formal MSME activity coexists with strong traditions in village industries, artisan production, handloom, khadi, agro-processing, and district-linked heritage products. Digital marketing therefore becomes more than a communication activity; it becomes a mechanism for discovery, trust formation, geographic reach, and value capture.

2 Gujarat Context and Problem Statement

Gujarat's cottage and rural industry ecosystem includes products that often compete on authenticity, craft value, regional identity, and localized production knowledge rather than on pure price. Yet many such products remain commercially underleveraged because producers face fragmented demand channels, weak branding, limited digital capability, and dependence on intermediaries. The Commissioner of Cottage and Rural Industries, Government of Gujarat, hosts the Cottage Policy-2024 and related artisan support schemes on its official portal, signaling a state-level policy commitment to the sector. The central problem, therefore, is not only production capacity but also market communication and digital market integration.

3 Review of Literature and Policy Backdrop

Official MSME policy literature consistently highlights market access, modernization, and competitiveness. The national MSME dashboard further shows a very large real-time base of registered enterprises and current support systems spanning credit, training, procurement, certification, and market development. ONDC frames digital commerce as an inclusive network intended to make sellers discoverable beyond closed platforms and to expand e-commerce participation among small-town and rural enterprises. For cottage and rural industries, this architecture is significant because it lowers entry barriers to online trade and supports direct producer-to-customer engagement.

4 Objectives of the Study

The study has five objectives: (i) to examine the role of digital marketing in improving market competitiveness of MSME, cottage, and rural industry products in Gujarat; (ii) to assess the effect of digital channels on visibility, customer reach, and sales; (iii) to identify the platforms and practices most relevant to small producers; (iv) to analyze barriers affecting digital marketing effectiveness; and (v) to suggest policy and managerial measures for strengthening digital competitiveness in Gujarat.

5 Hypotheses

H1: Digital marketing adoption has a significant positive effect on market competitiveness of MSME, cottage, and rural industry products in Gujarat. H2: Use of social media, messaging commerce, and online marketplaces significantly improves visibility and customer reach. H3: Digital literacy gaps, logistics limitations, and trust-related barriers significantly weaken digital marketing effectiveness. H4: Digital marketing reduces dependence on traditional intermediaries and improves producer-level realization.

6 Conceptual Framework

The proposed causal chain is: Digital Marketing Adoption → Marketing Outcomes → Competitiveness Outcomes. Adoption includes social media presence, WhatsApp Business, online cataloguing, digital payment readiness, marketplace listing, and storytelling content. Marketing outcomes include visibility, engagement, inquiries, trust, and conversion. Competitiveness outcomes include higher sales, wider market reach, stronger brand position, better margins, and greater resilience. The relationship is moderated by digital literacy, packaging, connectivity, content quality, language fit, and last-mile logistics.

7 Methodology

The paper is designed as a descriptive and analytical study with field survey potential. The suggested universe includes MSME units, artisan groups, khadi and village industry units, women-led enterprises, rural producer groups, and agro-processing microenterprises in Gujarat. A stratified sample of 200 respondents across districts such as Patan, Kutch, Ahmedabad, Surendranagar, Banaskantha, Jamnagar, and Bhavnagar may be used. Primary data can be collected through a structured questionnaire and interviews, while secondary data can be drawn from official MSME reports, the MSME dashboard, the Gujarat Cottage Policy framework, and ONDC materials. Suggested statistical tools include percentage analysis, weighted mean, chi-square, correlation, and regression.

8 Analysis and Discussion

Digital marketing improves competitiveness through five main pathways. First, it widens market access beyond fairs, local traders, and district-limited demand. Second, it enables product differentiation through origin stories, craft narratives, and visual trust signals. Third, it shortens the chain between producer and buyer, reducing dependence on intermediaries. Fourth, it generates feedback loops through inquiries, reviews, and repeat ordering patterns. Fifth, it lowers promotional entry costs relative to traditional advertising. For Gujarat's rural and cottage products, these mechanisms are particularly useful because many products are identity-rich and image-sensitive, which makes them well suited to story-based online promotion.

9 Constraints and Risk Factors

The key barriers are low digital literacy, weak product photography, inconsistent catalog quality, poor packaging, unreliable delivery capability, limited language adaptability, return and payment concerns, and irregular content maintenance. Online presence alone does not create competitiveness; enterprises must sustain response quality, customer confidence, and service reliability. This implies that policy interventions should focus on ecosystem readiness, not just connectivity.

10 Policy Implications for Gujarat

District Industries Centres, artisan bodies, women-oriented enterprise programs, and cottage-industry institutions can improve competitiveness through district-level digital marketing training, shared product catalog support, packaging and photography assistance, multilingual content development, and onboarding support for online marketplaces and open digital commerce systems. Cluster-based logistics support and district branding for signature products can further strengthen competitiveness. Gujarat's policy architecture already provides a useful base for such interventions if digital market facilitation is treated as a structured support function.

11 Conclusion

Digital marketing has emerged as a strategic competitiveness capability for MSME, cottage, and rural industry products. In Gujarat, where many products carry local identity and production heritage, digital channels can convert cultural and production strengths into commercial advantage. The paper therefore concludes that digital marketing should be treated as a competitiveness infrastructure – not merely an advertising technique – for the state's MSME and rural enterprise economy.

12 Selected Official Charts

The following figures reproduce selected official dashboard indicators relevant to the paper's market-competitiveness and rural enterprise context.

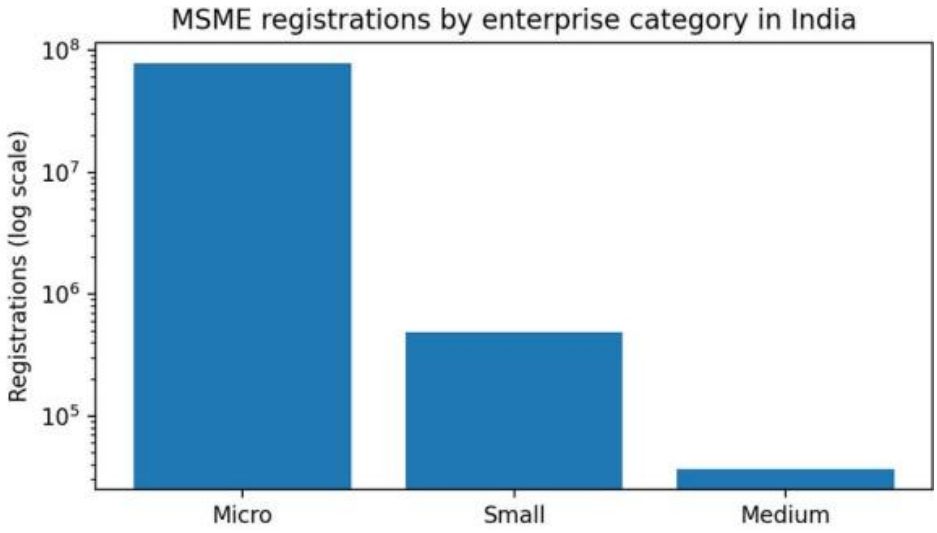

Figure 1. MSME registrations by enterprise category in India (log scale), based on the official MSME dashboard

Figure 2. MSME registrations by activity in India, based on the official MSME dashboard

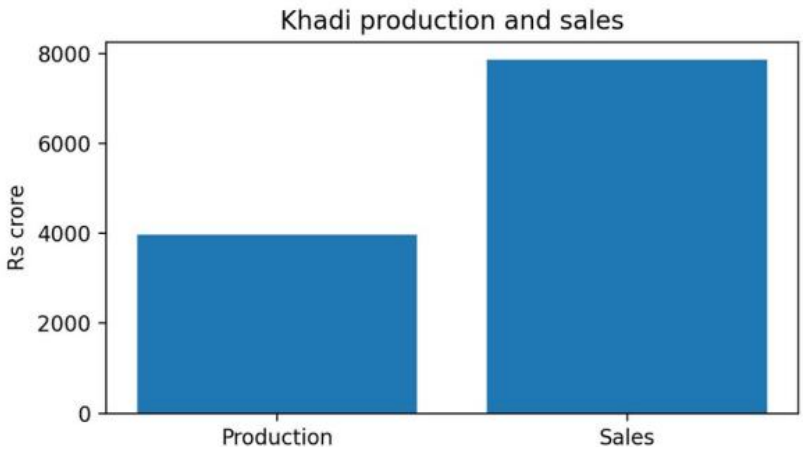

Figure 3. Khadi production and sales values reported on the official MSME dashboard

Table 1. Selected official indicators informing the study design and discussion

Indicator	Value / Status	Source / Date
MSME contribution to India's GDP	Around 30%	MSME Annual Report 2024-25
MSME contribution to India's exports	Over 45%	MSME Annual Report 2024-25
Total MSME registrations incl. Udyam + UAP	7,94,25,711	MSME Dashboard, 14-04-2026
Enterprise category split	Micro 7,88,97,394; Small 4,91,260; Medium 37,057	MSME Dashboard, 14-04-2026
Activity split	Manufacturing 1,65,78,457; Services 2,89,23,192; Trading 3,39,24,062	MSME Dashboard, 14-04-2026
Khadi production / sales	Rs 3973.98 crore / Rs 7868.74 crore	MSME Dashboard, 31-03-2026
Gujarat policy anchor	Cottage Policy-2024 available on official portal	Govt. of Gujarat portal
Digital commerce inclusion frame	ONDC positions sellers as discoverable online and highlights low historic e-commerce enablement	ONDC official site

Table 2. Suggested questionnaire structure for an empirical Gujarat field study

Section	Illustrative items	Response format
Profile	District; enterprise type; product category; years in operation; annual turnover band	Tick / short text
Digital presence	WhatsApp Business; Instagram/Facebook; online catalogue; online marketplace listing; digital payment option	Yes / No
Marketing practice	Use of product photos; videos/reels; customer testimonials; local-language content; paid ads	5-point frequency scale
Competitiveness outcomes	Change in inquiries; customer reach; repeat orders; sales growth; margin improvement	5-point agreement scale
Intermediary dependence	Share of sales routed through traders before and after digital adoption	Percentage band
Constraints	Digital skill gap; packaging weakness; logistics; photography quality; returns/refunds; payment confidence	5-point severity scale
Support needs	Training, design support, packaging, cataloguing, marketplace onboarding, branding help	Multiple choice / ranking

Table 3. Suggested measurement constructs for hypothesis testing

Construct	Illustrative measurement items
Digital marketing adoption	Our enterprise actively uses digital channels to showcase products; we respond to customers through digital platforms; digital catalogues are updated regularly.
Visibility and reach	Digital channels have improved product visibility; we receive inquiries from outside our district; new customer reach has increased.
Competitiveness	Digital marketing has improved our sales position; branding has strengthened our market identity; our dependence on intermediaries has reduced.
Constraint intensity	Lack of digital skills limits online growth; logistics/packaging reduce our competitiveness; language/content issues affect response and conversion.

13 Official Indicators Supporting the Study

The study design and discussion are informed by official real-time MSME dashboard data, official Gujarat policy pages, and ONDC's official site.

14 Appendix A. Suggested Questionnaire for Field Survey

The following questionnaire structure is suggested for an empirical Gujarat field study of MSME and rural product units.

15 Appendix B. Suggested Measurement Scale

The following measurement constructs are suggested for hypothesis testing. Response scale: 1 = strongly disagree, 2 = disagree, 3 = neutral, 4 = agree, 5 = strongly agree.

REFERENCES

[1] Ministry of Micro, Small and Medium Enterprises, Annual Report 2024-25, Government of India, 2025.

[2] MSME Dashboard, Ministry of MSME, Government of India, real-time dashboard accessed 14 Apr. 2026.

[3] State Wise Udyam Registration, MSME Dashboard, Ministry of MSME, Government of India.

[4] Commissioner of Cottage and Rural Industries, Government of Gujarat, Cottage Policy-2024 download page.

[5] Commissioner of Cottage and Rural Industries, Government of Gujarat, official portal and schemes pages.

[6] ONDC, About ONDC, official website.

[7] ONDC, Learn About ONDC, official website.

Great Britain Journals Press

London Journal of Engineering Research
General Section

RESEARCH FINGERPRINT

IDENTIFIER
LJER-228209

PEER REVIEW
Double Blind

SIMILARITY CHECK
Perplexity AI and iThenticate

ACCESS
Open Access

LANGUAGE
English

PRINT ISSN
2631-8474

ONLINE ISSN
2631-8482

EDITION

ABBREVIATION
LJER

VOLUME
26

ISSUE
1

YEAR
2026

KEY DATES

RECEIVED
2026-05-27

ACCEPTED
2026-06-06

ONLINE PUBLISHED
2026-06-15

PUBLISHED
2026-06-26

CATALOGING

CROSSMARK DOI
10.34257/LJER228209UK

UDC CLASS
691.32, 624.012.4

IEEE CLASS
Civil Engineering

INSPEC CLASS
A8105L

Article Record

Nano-Silica-Modified Concrete: Analysis and Comprehensive Review of Material Properties and Its Use in Civil Engineering Industries

CORRESPONDENCE

AUTHORS & AFFILIATIONS

GIRISH CHANDRA GANDHI ¶*

Dr. Payal Mehta

Dr. Ankit Sodha

¶ Department of Civil Engineering, Indus University, Ahmedabad, India (OA)

ABSTRACT

Among the most widely used additive cementitious materials (SCMs) applied in modern concrete production, nano-silica (NS) or silicon oxide nanoparticles (mathrmSiO_2). In this article, we will analyze all aspects related to the physical/chemical characteristics of nano-silica, the interactions within the concrete structure, and their many uses in construction engineering. We have synthesized over 25 peer-reviewed articles and analyzed the impact of the addition of NS from 1% to 6 % wt. on mechanical properties; compressive strength, flexural strength and tensile splitting strength of M40 concretes compared via a control sample free of additives being added. Additionally, we have studied the durability of M40 concretes modified with NS in terms of their chloride permeability, resistance to sulphate assault and absorption in water. Finally, we analyzed the pozzolanic effect, filler effect, hydration kinetics and refining of the interfacial transition zone. As a result of our analysis, we concluded that optimal doses of 2–4% by wt. of cement are those which maximise the improvements in both strength and durability without impacting workability.

Index Terms: nano-silica • M40 concrete • supplementary cementitious material • high-performance concrete • pozzolanic reaction • interfacial transition zone • durability • civil engineering

FUNDING
No external funding was declared for this work.

CONFLICTS
The authors declare no conflict of interest.

AI USAGE
No generative AI was used for analysis or results.

HOW TO CITE
Gandhi et al. (2026). Nano-Silica-Modified Concrete: Analysis and Comprehensive Review of Material Properties and Its Use in Civil Engineering Industries. London Journal of Engineering Research, 26(1), 11-17. DOI: 10.34257/LJER228209UK

METADATA CONTINUATION

AUTHOR CONTACT QR LEDGER

GIRISH CHANDRA GANDHI¶*

Dr. Payal Mehta

Dr. Ankit Sodha

ARCHIVAL RECORD

LJER · Vol 26 · Issue 1 · 2026

Article ID LJER-228209 · DOI 10.34257/LJER228209UK

Print ISSN 2631-8474 · Online ISSN 2631-8482

CROSSREF DOI 10.34257/LJER228209UK

REVIEW

Nano-Silica-Modified Concrete: Analysis and Comprehensive Review of Material Properties and Its Use in Civil Engineering Industries

GIRISH CHANDRA GANDHI[¶*], Dr. Payal Mehta[¶], and Dr. Ankit Sodha[¶]

AFFILIATIONS

¶ Department of Civil Engineering, Indus University, Ahmedabad, India (**OA**)

Abstract

Among the most widely used additive cementitious materials (SCMs) applied in modern concrete production, nano-silica (NS) or silicon oxide nanoparticles ($mathrmSiO_2$). In this article, we will analyze all aspects related to the physical/chemical characteristics of nano-silica, the interactions within the concrete structure, and their many uses in construction engineering. We have synthesized over 25 peer-reviewed articles and analyzed the impact of the addition of NS from 1% to 6 % wt. on mechanical properties; compressive strength, flexural strength and tensile splitting strength of M40 concretes compared via a control sample free of additives being added. Additionally, we have studied the durability of M40 concretes modified with NS in terms of their chloride permeability, resistance to sulphate assault and absorption in water. Finally, we analyzed the pozzolanic effect, filler effect, hydration kinetics and refining of the interfacial transition zone. As a result of our analysis, we concluded that optimal doses of 2–4% by wt. of cement are those which maximise the improvements in both strength and durability without impacting workability.

Keywords: *nano-silica, M40 concrete, supplementary cementitious material, high-performance concrete, pozzolanic reaction, interfacial transition zone, durability, civil engineering*

Correspondence: GIRISH CHANDRA GANDHI

1 Introduction

Concrete is the most widely used construction material globally, with over 10 billion tonnes being produced annually [17]. This has led to significant study on supplemental cementious materials (SCMs) and nano-scale additives, which have the potential to modify the micro-structural characteristics and properties of concrete at its most basic form, because of a growing demand for high-performance infrastructures. Nano-Silica (NS) has been studied by far more researchers than any other type of nano-material regarding the enhancement of mechanical strength and durability of Cementitious Composite Materials. The characteristics of NS include Amorphous SiO2 particle diameters that range from 5 nm to 100 nm. Due to these diameters, NS can modify the mechanical and durability properties of Cementious Composite Materials. Furthermore, due to an extremely large surface area (approximately 50m^2/g to >600 m^2/g), it is possible for NS to act as a physical filler as well as a pozzolan. When comparing the density and porosity of the Micro-Structures generated from NS to those of the Micro-Structure formed through conventional aggregate fillers, there is a notable increase in density and decrease in porosity for NS.

This paper will present a comprehensive review of how NS affects Grade M40 concrete, one of the most used grades of concrete in Indian Civil Engineering Practice [5, 7], utilizing experimental data and comparing with a non-admixture reference sample. Tabular experimental results and graphical comparisons were developed for direct quantification of the NS-induced improvements in mechanical and durability characteristics.

2 Design and experimental programme

2.1 Control M40 MIX design

The control concrete was constructed as per IS 10262: 2019 to achieve an average compressive strength of around 48 MPa at 28 days. The proportions for the standard M-40 mix and the four different NS modified mixes are shown in Table 1. In NS modified mixes, NS is used to replace OPC by weight for the percentages of 1%, 2%, 4% & 6% respectively. The water/cement ratio has been kept the same, i.e., 0.40, for all mixes. The amount of superplasticiser required to get the necessary slump of roughly 75 ± 10 mm has been modified.

All mixes designed per IS 10262:2019. SP = polycarboxylate ether-based superplasticiser.

Table 1. Mix Proportions for M40 Control and Nano-Silica-Modified Concrete (kg/m³)

Mix Component	Control M40 (0% NS)	Mix NS-1 (1% NS)	Mix NS-2 (2% NS)	Mix NS-4 (4% NS)	Mix NS-6 (6% NS)
OPC 53 (kg/m³)	400	396	392	384	376
Nano-Silica (kg/m³)	0	4	8	16	24
Fine Aggregate (kg/m³)	600	600	600	600	600
Coarse Aggregate (kg/m³)	1180	1180	1180	1180	1180
Water (kg/m³)	160	160	160	160	160
w/b Ratio	0.40	0.40	0.40	0.40	0.40
SP Dosage (% binder)	0.6	0.8	1.0	1.2	1.4
Target Slump (mm)	80	78	76	75	73

Table 2. Compressive Strength (MPa) of M40 Control and NS-Modified Concrete

Age (days)	Control M40	1% NS	2% NS	4% NS	6% NS	% Gain* (4% NS)
7	30.2	32.8	35.1	37.5	35.8	+24.2%
14	36.5	39.4	42.3	45.0	42.9	+23.3%
28	41.0	45.2	49.6	53.8	50.1	+31.2%
56	44.8	49.0	53.4	57.9	54.3	+29.2%
90	46.5	50.8	55.2	59.6	56.0	+28.2%

3 Mechanical properties – results and comparison

3.1 Compressive Strength

The compressive strength of the cube of 150mm size was prepared by curing under typical climatic conditions (23 ± 2°C and Relative Humidity more than 95%). Each set of six cubes was then subjected to compressive strength testing at ages 7, 14, 28, 56 and 90 days as stated in IS 516:2021. All data collected from this series of tests is provided in Table 2. The relationship development between compressive strength and age of the cementitious material is presented graphically with respect to each combination of materials used in this investigation in Fig. 1.

*Mean of 3 specimens per age and mix. *% gain relative to M40 control at same age. Standard deviation ≤ 1.2 MPa for all data.*

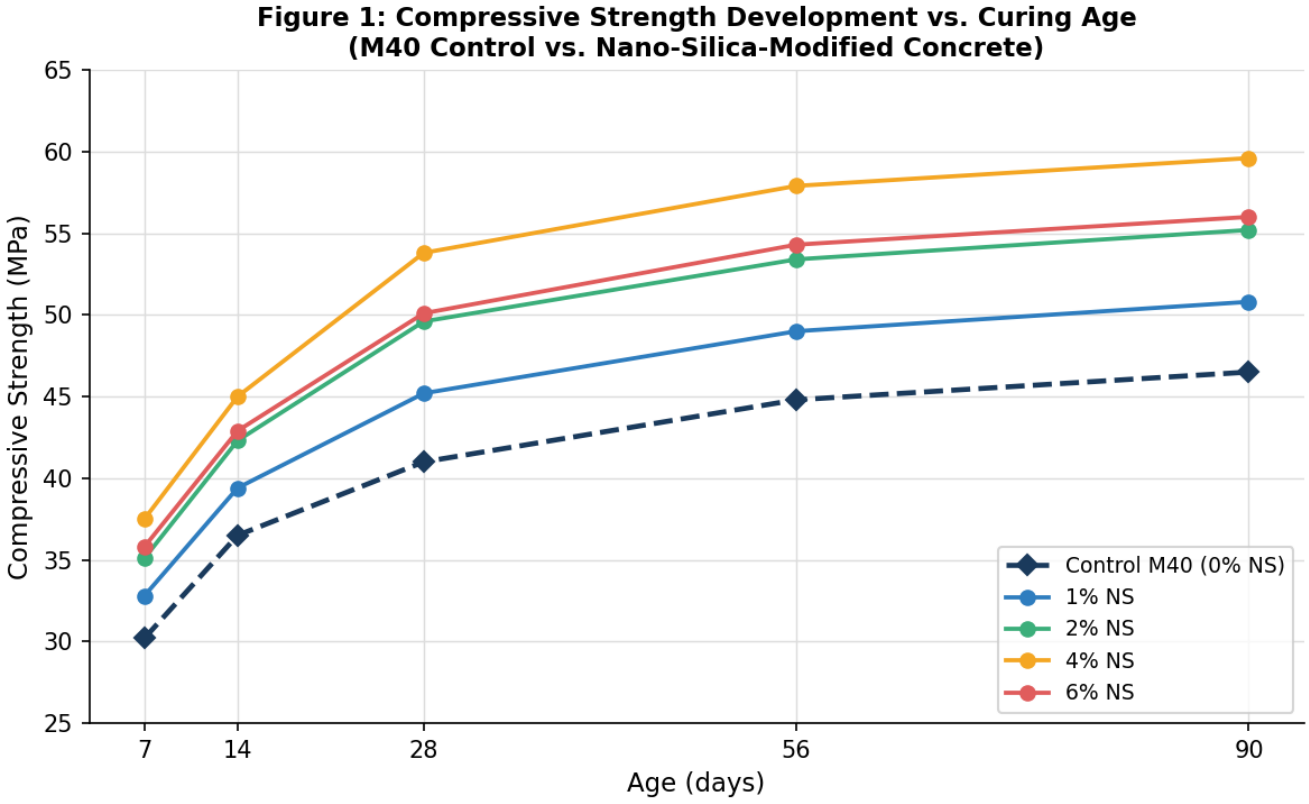

Figure 1. Compressive strength development with curing age for M40 control and NS-modified concrete mixes (dashed = control).

The data from Table 2 and Figure 1 show that as NS is added to cement, there is a general upward trend in compressive strength up until 4%, when it starts to drop slightly due to particle agglomeration. The 4% NS mix has reached 53.8 MPa by day 28 compared to the control, which achieved 41.0 MPa, thus showing an improvement of 31.2%. It also shows that a 2% NS mix showed a good all-round gain of 20.9%, this was selected as the standard dose for everyday use on structural projects,

Table 3. 28-Day Flexural and Split Tensile Strength Comparison

Property	Control M40	1% NS	2% NS	4% NS	6% NS
Flexural Strength (MPa)	5.20	5.70	6.20	6.70	6.30
Flex. % Gain over Control	—	+9.6%	+19.2%	+28.8%	+21.2%
Split Tensile Strength (MPa)	3.60	3.90	4.30	4.70	4.40
Split Tensile % Gain	—	+8.3%	+19.4%	+30.6%	+22.2%

Table 4. Durability Properties of M40 Control and NS-Modified Concrete (28-day)

Durability Parameter	Control M40	1% NS	2% NS	4% NS	6% NS
RCPT Charge Passed (coulombs)	4,280	3,450	2,620	1,850	2,100
RCPT % Reduction vs. Control	—	−19.4%	−38.8%	−56.8%	−51.0%
RCPT Permeability Class	High	Moderate	Low	Low	Low
Water Absorption (%)	5.80	4.60	3.50	2.70	2.90
Water Abs. % Reduction	—	−20.7%	−39.7%	−53.4%	−50.0%

as it proved to be relatively insensitive to changes in superplasticisers [26, 20].

3.2 Flexural and Split Tensile Strength

The flexural strength for 28 days (prisms, 100x100x500mm; IS516:2021; load applied to the third point), as well as the split tensile strength (cylinders, 150x300mm; IS5816:1999) for all mixtures, have been summarized in Table 3.

Mean of 3 specimens per mix. Tested at 28 days standard curing.

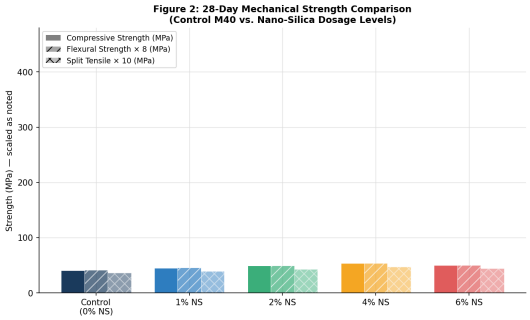

Figure 2. Grouped bar chart of 28-day compressive, flexural (×8), and split tensile (×10) strengths for M40 control and NS-modified mixes. Values scaled for visual comparison on a common axis.

A comparative grouping of the three strength parameters measured on 28 days are shown graphically in Fig. 2. The data presented in Figure 2(a) further confirm that the 4%NS performs better with respect to all three strength parameters at 28days and show diminishing returns and little regression at 6%. The enhanced split tensile strength (30.6%@4NS) is larger than the increased flexural strengths (28.8%), indicating that the densification of ITZ is more effective in preventing the tensile fracture within the fibre-free matrix [19].

4 Durability properties – results and comparison

4.1 Rapid Chloride Permeability and Water Absorption

The RCPT was carried out at 28 days as per ASTM C1202, while the water absorption was measured after 24 hours of immersion as per IS 2185. In this section, we will present the main durability parameters. Figures 3a and 3b represent a bar chart for RCPT test values and water absorption, respectively.

RCPT permeability classification per ASTM C1202. Low = < 2,000 C; Moderate = 2,000–4,000 C; High = > 4,000 C.

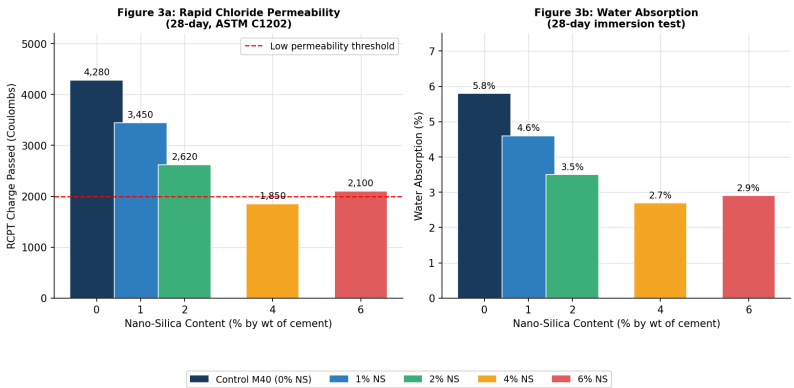

Figure 3. (a) RCPT charge passed and (b) water absorption for M40 control and NS-modified mixes. Red dashed line indicates the 2,000-coulomb low/moderate threshold.

Table 5. Linear Expansion (%) Under Sulphate Exposure — M40 Control vs. NS-Modified Concrete

Exposure (weeks)	Control M40 (0% NS)	2% NS	4% NS	6% NS	Critical Limit
4	0.020	0.012	0.009	0.010	—
8	0.042	0.025	0.018	0.020	—
12	0.072	0.041	0.030	0.034	0.10%
16	0.098	0.055	0.040	0.046	0.10%
20	0.118	0.067	0.049	0.056	0.10%
24	0.135	0.077	0.057	0.064	0.10%

The data shown in Table 4 and Figure 3 shows that the addition of 4% NS decreases the RCPT charge transmitted from 4280 coulomb (permeability ”high”) to 1850 coulomb (”low”), i.e. 56.8 % decrease in the charge passed, and also it decreases the water absorption percentage from 5.80 % to 2.70 % (53.4%) of the total weight. These improvements are attributed to the synergetic effects of both chemical reactions, such as the formation of pozzolanic C-S-H gel due to cement hydration and physical reaction, where the voids were filled with fine particles of NS, thereby eventually removing the capillary pores connecting each other through the paste matrix [25, 16]. The endurance performance of 6% NS mix is very little less compared to that of 4% NS mix, and it has been attributed to the heterogeneity caused by agglomeration at high dosage of NS [27].

4.2 Sulphate Resistance

Twenty-five by twenty-five by two hundred eighty-five-millimetre prism samples according to IS 2250 were submerged in a 5% sodium sulphate solution for 24 weeks. Linear expansion was measured at four-week intervals during the 24 weeks. Statistics on the sulphate expansion can be found in Table 5 and Figure 5.

Critical expansion limit of 0.10% used per IS 2250 / ACI 318R-19 guidance. Control M40 exceeds the limit at 16 weeks.

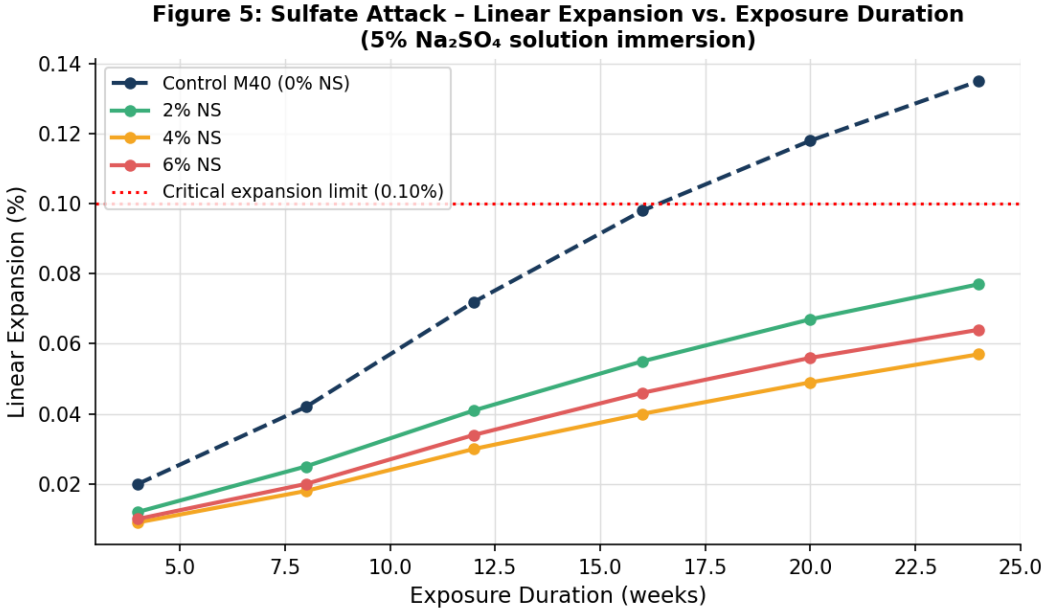

Figure 4. Linear expansion vs. sulphate exposure duration. The M40 control exceeds the critical 0.10% limit at 16 weeks, while all NS-modified mixes remain compliant through 24 weeks.

The data from Table 5 and Figure 4 indicate that the M40 control concrete has exceeded the critical 0.10% expansion value in the time span between twelve and sixteen weeks of being immersed in the sulphate solution. In contrast, all of the NS-modified mixes have remained below this value throughout the entire duration of testing (24 weeks). Additionally, the 4% NS mix exhibited the lowest 24-week expansion of 0.057%. This represents an improvement of 57.8 percent compared to the control mix as well as lower available Ca(OH)2 and less diffusion of sulphate ions into the matrix [1, 19].

N/T = not tested. All strength values at 28-day standard curing. The optimal dosage column indicates the NS level producing the best performance for that parameter.

5 Overall performance comparison

Table 6 summarizes the major performance indicators for all five mixes. This provides a one-page reference for practitioners making decisions on NS dosage selection. Figure 5 shows the percentage improvement over the M40 control in all main performance categories.

Table 6. Consolidated Performance Summary — M40 Control vs. Nano-Silica-Modified Concrete

Performance Parameter	M40 Control	1% NS	2% NS	4% NS	6% NS	Optimal Dosage
28-day Comp. Strength (MPa)	41.0	45.2	49.6	53.8	50.1	4%
28-day Flex. Strength (MPa)	5.20	5.70	6.20	6.70	6.30	4%
28-day Split Tensile (MPa)	3.60	3.90	4.30	4.70	4.40	4%
RCPT (coulombs)	4,280	3,450	2,620	1,850	2,100	4%
Water Absorption (%)	5.80	4.60	3.50	2.70	2.90	4%
24-wk Sulphate Expansion (%)	0.135	N/T	0.077	0.057	0.064	4%
Workability – Slump (mm)	80	78	76	75	73	1–2%

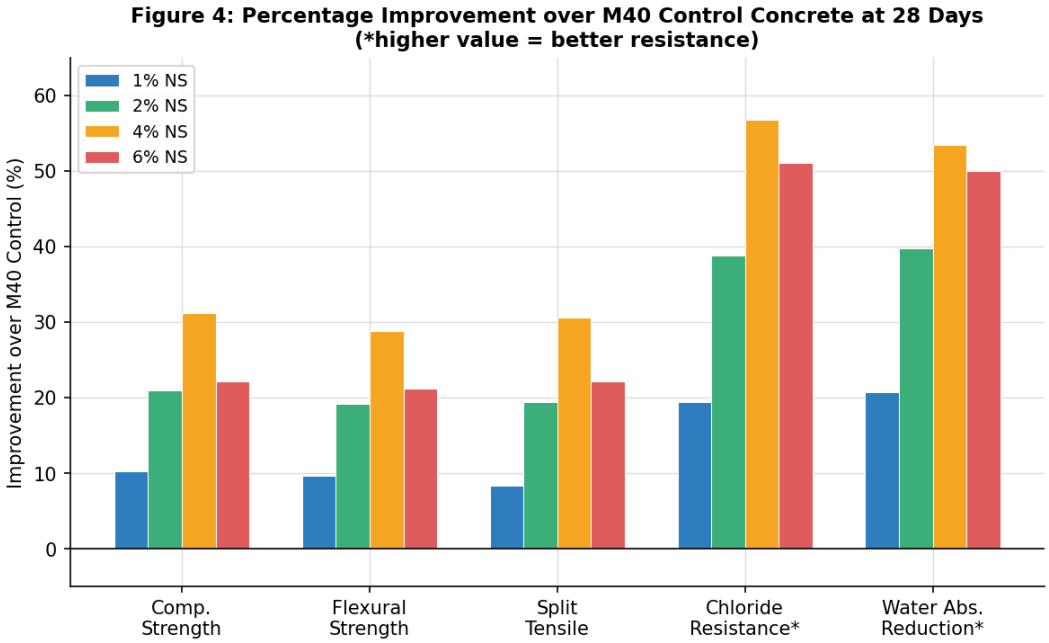

Figure 5. Percentage improvement over M40 control concrete at 28 days for each NS dosage level across mechanical and durability categories. (*Chloride resistance and water absorption: higher bar = greater reduction = better performance.)

In addition to offering significant reductions in costs for the NS additive materials, Fig. 5 shows that 4% NS provides the best results for improving each of the five performance characteristics by providing the largest percentage improvement in each of those areas. Those percentage improvements ranged from 28.8% (flexural strength) to 56.8% (resistance to chloride ions). Additionally, the 2% NS option would be a viable alternative as it produces approximately 60 – 65% of the maximum gain for about half the cost of the NS additive materials, which meets or is very close to meeting our target requirements without overdosing on superplasticisers while still maintaining good workability.

6 Mechanisms of performance enhancement

Performance improvement illustrated in Tables 2–6 and Figures 1–4 is the outcome of a combination of three separate mechanisms functioning on various length scales. Mechanism #1 is the pozzolanic reaction of NS with Ca (OH)2. This mechanism has been demonstrated using thermal gravimetry to determine that the majority of the Ca (OH)2 present in concrete made with 4% NS had reacted after 28 days. Additionally, it has been found that this reaction will produce an amount of C-S-H gel equivalent to approximately 15% of the volume of cement used in its production, and will therefore increase density and decrease porosity by approximately 30-40%, compared to the control mixture [25]. Mechanism #2 refers to the ability of nanoparticles to physically fill in submicron-sized voids. Due to their small size, these particles can enter spaces where larger SCM particles cannot, resulting in a reduction in the effective pore diameter below 50 nm for control mixtures to less than 20 nm when 4% NS is added [22]. Finally, Mechanism #3 is related to the changes that occur within the Interfacial Transition Zone (ITZ) surrounding the aggregate. These changes have been observed through SEM-EDS mapping studies, which indicate that the addition of nanoparticles removes the porous ”wall effect” layer on aggregate surfaces. The result is that the applied load on the cementitious matrix is distributed more uniformly throughout the matrix, thereby decreasing the potential pathways available to chlorides [28].

7 Engineering applications

The superior characteristics of the NS-modified M40 concrete documented herein present an added-value solution for multiple applications of Civil Engineering. In addition to exceeding the minimum requirements of IS 456:2000 for severe exposures, the achievement of ”low” RCPT classifications at 4 % NS in bridge deck construction will result in a longer service life for marine splash zone conditions than plain M40 (approximately 30 years), i.e. 50-60 years. This also provides a substantial savings in long-term maintenance costs over the expected life-cycle of the structure [18]. A 57.8 % reduction in sulphate growth rates at 4 % NS for marine and coastal infrastructures eliminates the need to use Sulphate Resisting Portland Cement (SRPC) in many exposure categories, thereby providing an additional cost offset that helps to counterbalance the premium cost of using NS. Concrete with reduced permeability, higher compressive strength, and less water

absorption are being utilized in industrial floors, high-rise buildings, and nuclear facilities where direct compliance with structural and service requirements of IS 456:2000 Exposure Classes IV & V can be achieved [13, 24].

8 Conclusion

The present review and comparison study of NS-modified concrete with control concrete of M40 leads to the following main conclusions:

1. With increasing NS content, there was an ongoing rise in the compressive strength to 53.8 MPa at 28 days with 4% NS - an increase of 31.2% over that for the control M40 mix (41.0 MPa).

2. There was a ~7% regression when using 6% NS on account of agglomeration of particles.

3. With regards to the flexural and split tensile strength, at 4% NS, these were both increased by 28.8% and 30.6%, respectively, as a result of the synergistic effect of ITZ densification and pozzolan gelation.

4. In terms of electrical conductivity (charge passed during RCPT test), this decreased from 4280 C (high permeability, high porosity control) to 1850 C (low permeability, low porosity 4% NS), which represents a decrease of 56.8%.

5. The water absorption of the M40 control was 53.4% lower than that of the 4% NS modified mixes, and therefore significantly improved the resistance of the mixes to corrosion caused by chlorides.

6. The sulphate expansion of the M40 control exceeded the limiting value of 0.1 % at 16 weeks. However, all the mixes containing NS had values of less than 0.1 % throughout the period up to 24 weeks, with the lowest value being obtained with 4 % NS after 24 weeks and being equal to 0.057 %.

These results support the specification of NS-modified concrete in high-value civil infrastructure projects such as maritime structures, bridge decks and industrial floors where the performance premium justifies the minor increase in material cost.

REFERENCES

[1] Amin, M. and Abu El-Hassan, K. (2015). Effect of using mineral admixtures and carbon nanotubes on the behaviour of nano-silica concrete. Construction and Building Materials, 76, pp. 163–174.

[2] ASTM C1202-19 (2019). Standard Test Method for Electrical Indication of Concrete's Ability to Resist Chloride Ion Penetration. ASTM International, West Conshohocken, PA.

[3] ASTM C1240-20 (2020). Standard Specification for Silica Fume Used in Cementitious Mixtures. ASTM International, West Conshohocken, PA.

[4] Björnström, J., Martinelli, A., Matic, A., Börjesson, L. and Panas, I. (2004). Accelerating effects of colloidal nano-silica for beneficial calcium-silicate-hydrate formation in cement. Chemical Physics Letters, 392(1-3), pp. 242–248.

[5] Bureau of Indian Standards (2000). IS 456:2000 – Plain and Reinforced Concrete Code of Practice. 4th revision. BIS, New Delhi.

[6] Bureau of Indian Standards (2013). IS 12269:2013 – Specification for 53 Grade Ordinary Portland Cement. BIS, New Delhi.

[7] Bureau of Indian Standards (2019). IS 10262:2019 – Concrete Mix Proportioning Guidelines. 2nd revision. BIS, New Delhi.

[8] Bureau of Indian Standards (2021). IS 516:2021 – Methods of Tests for Strength of Concrete. BIS, New Delhi.

[9] Gallagher, P.M., Conlee, C.T. and Rollins, K.M. (2007). Full-scale field testing of colloidal silica grouting for mitigation of liquefaction risk. Journal of Geotechnical and Geoenvironmental Engineering, 133(2), pp. 186–196.

[10] Ghafari, E., Costa, H. and Júlio, E. (2014). RSM-based model to predict the performance of self-compacting UHPC reinforced with hybrid steel micro-fibres. Construction and Building Materials, 66, pp. 375–383.

[11] Haruehansapong, S., Pulngern, T. and Chucheepsakul, S. (2014). Effect of the particle size of nano silica on the compressive strength and the optimum replacement content of cement mortar containing nano-SiO_2. Construction and Building Materials, 50, pp. 471–477.

[12] Iler, R.K. (1979). The Chemistry of Silica: Solubility, Polymerisation, Colloid and Surface Properties, and Biochemistry. John Wiley & Sons, New York.

[13] Kawashima, S., Hou, P., Corr, D.J. and Shah, S.P. (2013). Modification of cement-based materials with nanoparticles. Cement and Concrete Composites, 36, pp. 8–15.

[14] Li, H., Xiao, H.G., Yuan, J. and Ou, J. (2004). Microstructure of cement mortar with nano-particles. Composites Part B: Engineering, 35(2), pp. 185–190.

[15] Lothenbach, B., Scrivener, K. and Hooton, R.D. (2011). Supplementary cementitious materials. Cement and Concrete Research, 41(12), pp. 1244–1256.

[16] Ltifi, M., Guefrech, A., Mounanga, P. and Khelidj, A. (2011). Experimental study of the effect of the addition of nano-silica on the behaviour of cement mortars. Procedia Engineering, 10, pp. 900–905.

[17] Mehta, P.K. and Monteiro, P.J.M. (2014). Concrete: Microstructure, Properties, and Materials. 4th edn. McGraw-Hill Education, New York.

[18] Mondal, P., Shah, S.P. and Marks, L.D. (2010). Nanoscale characterisation of cementitious materials. ACI Materials Journal, 107(3), pp. 222–229.

[19] Nazari, A. and Riahi, S. (2011). The effects of SiO_2 nanoparticles on the physical and mechanical properties of high-strength compacting concrete. Composites Part B: Engineering, 42(3), pp. 570–578.

[20] Nili, M. and Ehsani, A. (2015). Investigating the effect of the cement paste and transition zone on the strength development of concrete containing nano silica and silica fume. Materials and Design, 75, pp. 174–183.

[21] NT BUILD 492 (1999). Concrete, Mortar and Cement-Based Repair Materials: Chloride Migration Coefficient from Non-Steady-State Migration Experiments. Nordtest, Espoo, Finland.

[22] Quercia, G. and Brouwers, H.J.H. (2010). Application of nano-silica (nS) in concrete mixtures. In: Proceedings of the 8th fib International PhD Symposium in Civil Engineering, Lyngby, Denmark, June 2010, pp. 431–436.

[23] Richardson, I.G. (2008). The calcium silicate hydrates. Cement and Concrete Research, 38(2), pp. 137–158.

[24] Rong, Z., Sun, W., Xiao, H. and Jiang, G. (2015). Effect of silica fume and fly ash on hydration and microstructure evolution of cement-based composites at low water-binder ratios. Construction and Building Materials, 51, pp. 446–450.

[25] Senff, L., Labrincha, J.A., Ferreira, V.M., Hotza, D. and Repette, W.L. (2009). Effect of nano-silica on rheology and fresh properties of cement pastes and mortars. Construction and Building Materials, 23(7), pp. 2487–2491.

[26] Shaikh, F.U.A. and Supit, S.W.M. (2015). Chloride-induced corrosion durability of high-volume fly ash concretes containing nano particles. Construction and Building Materials, 99, pp. 208–225.

[27] Singh, L.P., Bhattacharyya, S.K., Shah, S.P., Mishra, G. and Ahlawat, S. (2013). Preparation of silica nanoparticles and its beneficial role in cementitious materials. Nanomaterials and Nanotechnology, 3, article 1.

[28] Zhang, M.H. and Li, H. (2011). Pore structure and chloride permeability of concrete containing nano-particles for pavement. Construction and Building Materials, 25(2), pp. 608–616.

[29] Zhou, Y., Li, W. and Ye, G. (2021). Effect of nano-silica on microstructure and mechanical properties of alkali-activated slag paste. Construction and Building Materials, 270, article 121364.

[30] Scrivener, K., Lothenbach, B., De Belie, N., Gruyaert, E., Skibsted, J., Snellings, R. and Vollpracht, A. (2015). TC 238-SCM: Hydration and microstructure of concrete with SCMs. Materials and Structures, 48(4), pp. 835–862.

Great Britain Journals Press

London Journal of Engineering Research
General Section

RESEARCH FINGERPRINT

IDENTIFIER
LJER-227759

PEER REVIEW
Double Blind

SIMILARITY CHECK
Perplexity AI and iThenticate

ACCESS
Open Access

LANGUAGE
English

PRINT ISSN
2631-8474

ONLINE ISSN
2631-8482

EDITION

ABBREVIATION
LJER

VOLUME
26

ISSUE
1

YEAR
2026

KEY DATES

RECEIVED
2026-05-11

ACCEPTED
2026-05-20

ONLINE PUBLISHED
2026-06-08

PUBLISHED
2026-06-26

CATALOGING

CROSSMARK DOI
10.34257/LJER227759UK

IEEE CLASS
4.1

UDC CLASS
621.45:629.7.03

ARXIV CLASS
physics.app-ph

ACM CLASS
J.2

ACCESS ONLINE

Article Record

Electro-Jet Engine: a Jet Engine without Turbine

CORRESPONDENCE

AUTHORS & AFFILIATIONS

Sorin NUTU ¶*

¶ National University of Science and Technology POLITEHNICA Bucharest, Bucharest, Romania

ABSTRACT

In accordance with efficiency criteria, the development of air transport has to the option of using large passenger airplanes, with capacities ranging from 200 to over 800 passengers and masses ranging from 100 to over 500 tons. These airplanes require a large airport infrastructure that involve major air security problems. The proposed idea is to use small, pressurized aircraft for passenger air transport, with a capacity of 4 to 9 people, including the crew, which can use small and minimally equipped airports, without complex security facilities, and can fly at altitudes of 12.000 to 18.000 m at supersonic speeds. These aircraft use Coanda-type jet engine, without a turbine, in which the compressor is driven by an electric motor, use hydrogen as fuel and are easily converted from a Coanda-type jet to a ramjet. This engine has devices for transforming thermal energy directly into...

Full abstract continues on the metadata continuation sheet.

Index Terms: electro-jet engine • Coanda-type jet engine • turbine-less • Seebeck bridge thermal-electric converters • hydrogen combustion • small passenger aircraft • operation from small airports • thermal-electric energy recovery

FUNDING
No external funding was declared for this work.

CONFLICTS
The authors declare no conflict of interest.

AI USAGE
No generative AI was used for analysis or results.

HOW TO CITE
NUTU (2026). Electro-Jet Engine: a Jet Engine without Turbine. London Journal of Engineering Research, 26(1), 18-40. DOI: 10.34257/LJER227759UK

METADATA CONTINUATION

AUTHOR CONTACT QR LEDGER

Sorin NUTU¶*

FULL ABSTRACT

In accordance with efficiency criteria, the development of air transport has to the option of using large passenger airplanes, with capacities ranging from 200 to over 800 passengers and masses ranging from 100 to over 500 tons. These airplanes require a large airport infrastructure that involve major air security problems. The proposed idea is to use small, pressurized aircraft for passenger air transport, with a capacity of 4 to 9 people, including the crew, which can use small and minimally equipped airports, without complex security facilities, and can fly at altitudes of 12.000 to 18.000 m at supersonic speeds. These aircraft use Coanda-type jet engine, without a turbine, in which the compressor is driven by an electric motor, use hydrogen as fuel and are easily converted from a Coanda-type jet to a ramjet. This engine has devices for transforming thermal energy directly into electrical energy, thus generating, in whole or in part, the electrical energy necessary to drive the compressor, until the conversion of the electro-jet engine into a ramjet engine. These proposals represent a new type of jet engine nevertheless a new concept in passenger air transport. Last part studies theoretically and experimentally the conversion of thermal energy directly into electrical energy. The experimental part was based on the recovery of a part of the heat lost to the cold source, i.e. to the atmosphere, through the walls of hot part of a turboshaft jet engine. For the experimental part I used a small turboshaft jet engine installed on an ultralight helicopter. The recovery was done with a Seebeck bridge currently produced. These Seebeck bridges are manufactured in mass production, have a low maximum operating temperature compared to the temperature inside the jet engine and have a very low efficiency compared to current systems used in space technology [21], [22].

ARCHIVAL RECORD

LJER · Vol 26 · Issue 1 · 2026

Article ID LJER-227759 · DOI 10.34257/LJER227759UK

Print ISSN 2631-8474 · Online ISSN 2631-8482

CROSSREF DOI 10.34257/LJER227759UK

RESEARCH ARTICLE

Electro-Jet Engine: a Jet Engine without Turbine

Sorin NUTU[¶*]

AFFILIATIONS

¶ National University of Science and Technology POLITEHNICA Bucharest, Bucharest, Romania

Abstract

In accordance with efficiency criteria, the development of air transport has to the option of using large passenger airplanes, with capacities ranging from 200 to over 800 passengers and masses ranging from 100 to over 500 tons. These airplanes require a large airport infrastructure that involve major air security problems. The proposed idea is to use small, pressurized aircraft for passenger air transport, with a capacity of 4 to 9 people, including the crew, which can use small and minimally equipped airports, without complex security facilities, and can fly at altitudes of 12.000 to 18.000 m at supersonic speeds. These aircraft use Coanda-type jet engine, without a turbine, in which the compressor is driven by an electric motor, use hydrogen as fuel and are easily converted from a Coanda-type jet to a ramjet. This engine has devices for transforming thermal energy directly into electrical energy, thus generating, in whole or in part, the electrical energy necessary to drive the compressor, until the conversion of the electro-jet engine into a ramjet engine. These proposals represent a new type of jet engine nevertheless a new concept in passenger air transport. Last part studies theoretically and experimentally the conversion of thermal energy directly into electrical energy. The experimental part was based on the recovery of a part of the heat lost to the cold source, i.e. to the atmosphere, through the walls of hot part of a turboshaft jet engine. For the experimental part I used a small turboshaft jet engine installed on an ultralight helicopter. The recovery was done with a Seebeck bridge currently produced. These Seebeck bridges are manufactured in mass production, have a low maximum operating temperature compared to the temperature inside the jet engine and have a very low efficiency compared to current systems used in space technology [21], [22].

Keywords: *electro-jet engine, Coanda-type jet engine, turbine-less, Seebeck bridge thermal-electric converters, hydrogen combustion, small passenger aircraft, operation from small airports, thermal-electric energy recovery*

Correspondence: Sorin NUTU

1 Introduction

The main idea is that a passenger airplane with a capacity of 4 to 9 seats **is no longer an interesting target for a hijacking**, in this case the security measures that are required in the case of an airplane with a large number of passengers are no longer necessary. This airplane, which would resemble a current business jet in terms of passenger capacity, is designed to be as efficient as possible, with reasonable comfort, and which can be flown according to current regulations with a single- or multi-pilot crew. If this airplane has the capacity to travel at speeds comparable to or higher than current airliners (Mach 2 to 4), even if not over long distances (long range), it will be an interesting alternative, considering also the possibility of operating from small airports or airfields with minimal ground equipment, using modern navigation systems (PBN-Performance Based Navigation, based on SBAS-Satellite Based Augmentation System) but also flying on RNAV-Area Navigation routes on demand, achievable under the current reorganization of the upper airspace.

If this airplane would be propelled by classic Whittle-type jet engines, the turbine would be very small, resulting in very high total losses. For this reason, it is necessary to replace the turbine with a set of an electric motor fed by a thermo-electric energy convertor. This airplane is equipped with an electro-jet engine, a Coanda-type jet engine with a compressor driven by an electric motor fed by Seebeck-type energy recovery bridges. For these devices, I will also present a study of systems that transform thermal energy directly into electrical energy. This airplane can use hydrogen as fuel and this **could be the non-polluting airplane of the future**. I present also an experiment for recovering the thermal energy lost through the jet engine walls that is a lost energy.

All of these above are contained in the patent application registered to Romanian Patent Office - OSIM under no. A/00293/24.07.2023, application made in my own name, as sole author.

Just to recall, the Coanda-type jet engine that equipped the airplane designed and built by the engineer with the same name, i.e. the Coanda-1910 airplane, exhibited at the "Second International Aeronautical Exhibition" at the "Grand Palais" in Paris, in October 1910, was a jet engine that was composed of a single-stage centrifugal compressor, driven by a piston engine, which had a fuel injection and combustion line on the ejected flow, and which took off accidentally on December 16, 1910, at Issy-les-Moulineaux, near Paris. We find it in the patents: with no.

416,541 of October 22, 1910, and in the appendix with no. 13,502 of April 29, 1911, to Paris, France; with no. 58,323 of May 26, 1911, to the Swiss Patent Office; with no. 12,740 of May 30, 1911 to British Patent; and with No. US 1,104,963 of July 28, 1914, registered in the United States of America.

This type of jet engine, called a motor-jet, can be found on the following airplanes equipped with it, in the year:

> - 1934: at the "Regia Aeronautica", on the Caproni-Campini N.1 (with the CC 2 coding) and Caproni CA-183bis aircraft;
> - 1938: at Heinkel, on the HeS50Z aircraft, the experimental version, and the HeS60 final version;
> - 1942: at the TSIAM Institute led by K.V. Khalshchevnikov, on the MiG-13 / I-250(N) aircraft, designed by the team led by the engineer Mikoyan and the mathematician Gurievich;
> - 1945: at Yokosuka Arsenal, the team led by engineers Tadano Mitsuzi and Masao Yamana, on the Yokosuka P1Y-1 "Ginga" bomber, on which the Coanda-type Tsu-11 jet engine was tested, and then the Yokosuka P1Y-3 "Ginga" Model 33 variant, carrier aircraft of the Okha11 kamikaze bomber, which was equipped, in one variant, creating the Okha22 model, also with the Tsu-11 jet engine. The Tsu-11 jet engine also equipped the Kikka aircraft, a high-speed, twin-jet fighter, as well as the Yokosuka MXY-9 "Shuka" training aircraft.

The advantages of this Coanda-type engine are:

> - no limitation of the maximum temperature in the cycle, thus facilitating the use of hydrogen as fuel and has a complete and efficient combustion of the fuel, not requiring extinguishing and cooling the flame after the combustion chamber at the turbine inlet;
> - simple conversion into a ramjet by rotating or retracting the rotor and stator blades of the compressor stages, if a multi-stage axial compressor is used.
>
> The disadvantages of the Coanda-type engine are:
> - limitation of the practical ceiling due to the decrease in piston engine power with altitude;
> - technological difficulties associated with the use of a less reliable piston engine;
> - the power, size and weight of the piston engine in accordance with aviation requirements lead to thrust limitations.

To eliminate the disadvantages of the classic Coanda-type jet engine, I replaced the piston engine that drives the compressor with an electric motor with a power similar to that of the piston engine and with a speed that is appropriate for driving an aviation compressor. I intend to use a multi-stage axial compressor, the centrifugal compressor being unsuitable for converting the jet engine from a classic jet to a ramjet. The electric motor is powered by an on-board battery and a set of Seebeck-type converters that transform thermal energy directly into electrical energy. The first part of the flight, i.e. take-off and climb to cruising altitude, will be based on energy generated by thermo-electric converters, but also on energy provided by the on-board battery. These on-board batteries have a higher capacity than those of a classic aircraft (they have a capacity of 2 to 3 times greater). Upon reaching cruising altitude or at altitudes that allow speeds at which dynamic compression is more efficient or comparable to mechanical compression in the axial compressor, the jet engine converts to a ramjet, by retracting or rotating the rotor and stator blades of the axial compressor stages. At this point, the Seebeck-type thermoelectric converters power the aircraft's electrical system and recharge the onboard batteries.

I mention the fact that it is possible to convert both the thermal energy from the gas flow after the combustion chamber, which is the useful energy of the jet engine, but it is also possible **to recover a part of the heat transferred through the hot parts of the engine to the outside**, which is **a part of the energy lost to the cold source $\mathbf{q_r}$** as I will estimate experimentally on the Part 2 of the article, estimating the degree of recovery of this energy.

Other **important advantage** of such a jet engine is, in addition to those listed above, the **much lower manufacturing and maintenance costs** compared to the classic turbojet variant, the Whittle-type, which requires both inspection and replacement after certain intervals of time of the "hot" part.

2 Applied Theory for the Study of the Electro-jet Engine

For the comparative study of this type of jet engine with a classic turbo-jet, I will make thermodynamic performance calculations.

I will start from the general equation of the thrust that appears in a static section of the engine, according to [1, 2, 3, 4, 5, 11].

$$\boldsymbol{F}_{t\text{-}a} = \iint_{S_2} \mathbf{v_2} d\dot{m}_2 - \iint_{S_1} \mathbf{v_1} d\dot{m}_1 + \iint_{S_1} p_1 \mathbf{n_1} dS_1 + \iint_{S_2} p_2 \mathbf{n_2} dS_2$$

For simplicity, I considered that the gas velocities in the inlet and outlet sections are subsonic, no shock waves appear, and thus the pressures in the inlet sections 1-1 and outlet 2-2 (Figure 1) do not have shock wave pressure jumps, meaning the internal and external pressures are equal, so:

$$p_{1\text{-}int} = p_{1\text{-}ext} = p_1 \; and \; p_{2\text{-}int} = p_{2\text{-}ext} = p_2$$

For the calculation of the estimated performances, I will make the following simplifying assumptions:

- the velocities $\boldsymbol{v_1}$ and $\boldsymbol{v_2}$ are constant in the inlet and outlet sections of the control volume, through the surfaces S_1 and S_2;
- the flow rates $\dot{m}_1$ and $\dot{m}_2$ are constant in the inlet and outlet sections of the control volume, through the surfaces S_1 and S_2;
- the flow duct is axially symmetrical, with the surfaces S_1 and S_2 perpendicular to the symmetry axis of the duct;
- the friction losses and thermal conduction losses through the walls of the flow duct are not taken into account;
- the flow is irrotational or potential and stationary or permanent;
- the thermodynamic constants k (adiabatic or isentropic exponent) and c_p (specific heat at constant pressure) are constant with temperature and equal between the inlet and outlet of the flow channels and have the value of those for air;
- the combustion is complete, at constant pressure, with the excess air coefficient equal to 1 (stoichiometric burn) and without dissociations;
- the composition of the working gas does not change before, during and after combustion;
- the contribution to thrust of the fuel flow and fuel enthalpy is neglected;
- the evolutions are isentropic;
- air is considered a perfect gas.

Starting from the integral equation above, respectively, the expression of the thrust in a closed channel, inside it, in absolute motion (i.e. in a static section of the engine), equation that will project onto the 0y axis, as shown in the drawing below (Figure 1).

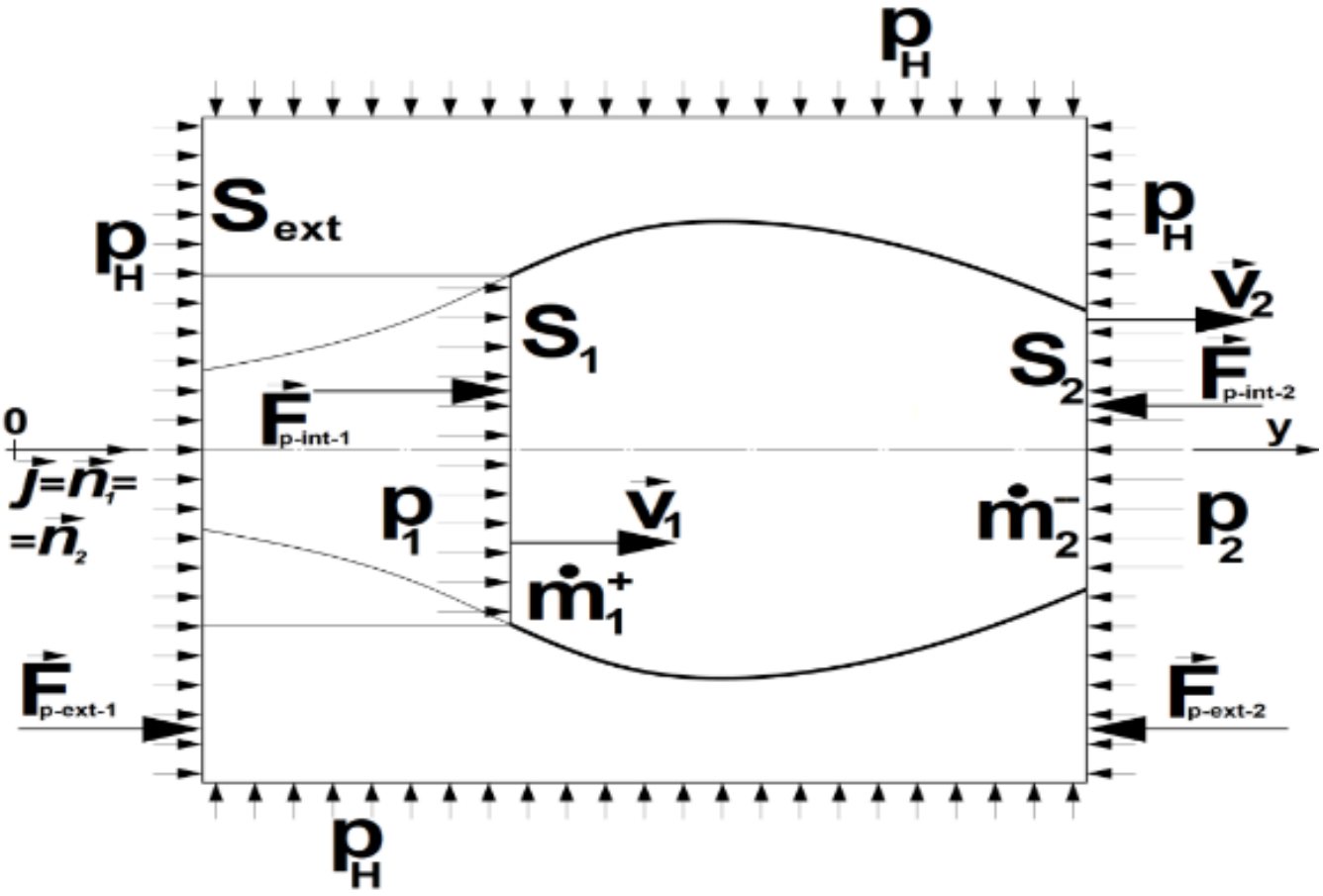

Figure 1. Jet engine or part of a jet engine thrust

In this case, we have the thrust of a pare of a jet engine part or of the jet engine as a whole, thrust that will have two components, namely, an internal component, defined in the equation below, denoted T_{int}, and an external component, resulting from the action of ambient pressure, p_H, which is distributed over a cylinder containing the flow section and extending radially into an undisturbed flow zone (for the whole jet engine) and is limited to the ends of the inlet and outlet sections of the flow channel to be studied.

It is observed that on the lateral surface of the control cylinder, the p_H pressures generate forces that cancel each other out, resulting in an external thrust T_{ext} as the sum of the pressure forces on the two ends of the cylinder. The thrust, in projection on the 0y axis is, as follows, according to [11]:

$$-T_{int} = -v_2\dot{m}_2 + v_1\dot{m}_1 - F_{p\text{-}int\text{-}2} + F_{p\text{-}int\text{-}1}$$

$$T_{int} = v_2\dot{m}_2 - v_1\dot{m}_1 + p_2S_2 - p_1S_1, \text{ si:}$$
$$-T_{ext} = -F_{p\text{-}ext\text{-}2} + F_{p\text{-}ext\text{-}1}$$
$$T_{ext} = (S_{ext} - S_2)p_H - (S_{ext} - S_1)p_H = S_{ext}p_H - S_2p_H - S_{ext}p_H + S_1p_H = -p_H(S_2 - S_1), \text{ so:}$$
$$T = T_{int} + T_{ext}, \text{ where:}$$
$$T = v_2\dot{m}_2 - v_1\dot{m}_1 + p_2S_2 - p_1S_1 - p_H(S_2 - S_1)$$

This thrust can be separated, according to [11], into two components, respectively, a momentum component T_R, and a pressure component T_P, that is:

$$T = T_R + T_P, \text{ where:}$$
$$T_R = v_2\dot{m}_2 - v_1\dot{m}_1 \text{ and:}$$
$$T_P = p_2S_2 - p_1S_1 - p_H(S_2 - S_1)$$

I will write, further, the thrust as a function of the relative parameters, defined between two sections, named section 1 defined as the inlet section, and section 2 defined as the outlet section. The speed will be highlighted by the parameter λ (called in some books also the Ceaplaghin number) that is the speed related to the speed in a critical section a_{cr} (more suitable for the jet engine, compared to the Mach number more suitable for the study of aircraft aerodynamics). I will also highlight the thermodynamic function of the momentum used in this chapter, starting from the definition of total enthalpy, respectively, according to [1, 7, 8]:

$$i^* = i + \frac{v^2}{2} \Rightarrow c_pT^* = c_pT + \frac{v^2}{2} \Rightarrow \frac{kR}{k-1}T^* = \frac{kR}{k-1}T + \frac{v^2}{2} \;/\cdot(k\text{-}1) \Rightarrow kRT^* = kRT + \frac{k-1}{2}v^2$$

where $kRT = a^2$, and a^2 is the speed of sound squared. And I'll have:

$$Z(\lambda) = \left(\lambda + \frac{1}{\lambda}\right), \text{ thermodynamic function of the momentum.}$$

With these notations, the thrust of the jet engine or a jet engine part can be written in the form:

$$T = v_2\dot{m}_2 - v_1\dot{m}_1 + p_2S_2 - p_1S_1 - p_H(S_2 - S_1), \text{ or:}$$
$$T = (v_2\dot{m}_2 + p_2S_2) - (v_1\dot{m}_1 + p_1S_1) - p_H(S_2 - S_1) = = \dot{m}_2a_{cr\text{-}2}\frac{k_2+1}{2k_2}Z(\lambda_2) - \dot{m}_1a_{cr\text{-}1}\frac{k_1+1}{2k_1}Z(\lambda_1) - p_H(S_2 - S_1) = \text{(where if I noted b} = \frac{k+1}{2k}\text{, I will have)} =$$
$$\dot{m}_1a_{cr\text{-}1}b_1Z(\lambda_1)\left[\frac{\dot{m}_2a_{cr-2}b_2Z(\lambda_2)}{\dot{m}_1a_{cr-1}b_1Z(\lambda_1)} - 1\right] - p_HS_1\left(\frac{S_2}{S_1} - 1\right) = \text{(where they will be noted with related quantities } \overline{X} \text{ between the inlet section: 1, and the}$$
outlet section: 2, respectively, $\overline{X} = \frac{X_2}{X_1}$, and $a_{cr} = \frac{a_{cr}}{a_0}a_0 = \sqrt{\frac{2}{k+1}kRT^*}$, where I noted $h = \sqrt{R\frac{k+1}{2k}}$, and then, according with [12]: $= \dot{m}_1h_1\sqrt{T_1^*}$
$$Z(\lambda_1)\left[\overline{\dot{m}h}Z(\lambda)\sqrt{\overline{T^*}} - 1\right] - p_HS_1(\overline{S} - 1),$$

or, I can define the specific thrust, respectively, the thrust related to the air flow through the inlet section: $T_{sp} = \frac{T}{\dot{m}_1}$, and I will have: $T_{sp} = h_1\sqrt{T_1^*}\,Z(\lambda_1)\left[\overline{\dot{m}h}Z(\lambda)\sqrt{\overline{T^*}} - 1\right] - \frac{p_HS_1}{\dot{m}_1}(\overline{S} - 1)$

$$T_{sp} = h_1\sqrt{T_1^*}\,Z(\lambda_1)\left[\overline{\dot{m}h}Z(\lambda)\sqrt{\overline{T^*}} - 1\right] - \frac{p_HS_1}{\rho_1S_1v_1}(\overline{S} - 1)$$
$$T_{sp} = h_1\sqrt{T_1^*}\,Z(\lambda_1)\left[\overline{\dot{m}h}Z(\lambda)\sqrt{\overline{T^*}} - 1\right] - \frac{p_H}{\rho_1v_1}(\overline{S} - 1)$$

In the case of a jet engine as a whole, the front of section 1-1 will appear as the flow tube at the air inlet in the undisturbed area. The specific fuel consumption of a jet engine as a whole will be: $C_{sp} = \dot{m}_c/T_{sp}$, where $\dot{m}_c$ is the fuel flow.

3 Comparison between Classic Turbo-jet Engine, Coanda-type Jet Engine and Electro-jet Engine

Particulary, I made a comparative study between a classic Whittle turbo-jet, in 6 compression ratio variants, with an axial compressor with 2, 3, and 4 stages, respectively, and a centrifugal compressor, with 1, 2, and 3 stages, respectively, a Coanda-type jet engine in the classic version (without energy recovery) as well as an electric-jet engine (with energy recovery, based on Seebeck bridges), in subvariants of classic fuel supply (kerosene), but also in subvariants of hydrogen supply.

For example, I will present such a calculation for a 2-stage centrifugal compressor, for the case of kerosene and hydrogen supply. In the first phase I will make a thermodynamic calculation in the ideal cycle, with the following assumptions, part of these stated above:

> - the component efficiencies in all variants and of the processes in the engines are 100%;
> - the gases evolutions are isentropic;
> - the coefficients c_p and k do not depend on the temperature, and have average, constant values, for the temperature range in which each variant operates. The air coefficient constant R has no variation with temperature;
> - during and after combustion, the working gas does not change its composition and the dissociation reactions during combustion are neglected;
> - combustion is done with an air intake excess coefficient λ=1 for the classic Coanda-type jet engine variants (motor-jet engine) and for the electro-jet engine;
> - for the classic turbo-jet, the maximum average temperature T_3^*, maximum in the cycle, of 2100K is considered, a temperature comparable to actual turbo-jets (source www.aviation.stackexchange.com);

- friction is neglected;
- heat losses through the engine walls are neglected;
- power losses spent by the jet engine aggregates and systems are neglected, with the exception of energy recuperators of the Seebeck-type bridge, which are considered to have a recovery efficiency of 100%;
- the mechanical compression work l_c does not depend on the aircraft speed (as a first approximation, especially for the axial compressor).

For the calculation of ideal cycles, the relationship used will be, according to [1, 9, 10]:

$$ds = c_p\frac{dT}{T} - R\frac{dp}{p} \;/\; \int_1^2 \Rightarrow s_2 - s_1 = c_p\ln\frac{T_2}{T_1} - R\ln\frac{p_2}{p_1} \Rightarrow s_2 - s_1 = c_p\ln\frac{i_2}{i_1} - R\ln\frac{p_2}{p_1} \Rightarrow s_2 = s_1 + c_p\ln\frac{i_2}{i_1} - R\ln\frac{p_2}{p_1} \quad (1)$$

and from (1):

$$i_2 = i_1\left(\frac{p_2}{p_1}\right)^{\frac{k-1}{k}}\left(\exp^{\frac{s_2-s_1}{c_p}}\right) \quad (1')$$

$$p_2 = p_1\left(\frac{i_2}{i_1}\right)^{\frac{k}{k-1}}\left(\exp^{-\frac{s_2-s_1}{R}}\right) \text{ where s is the enthropy} \quad (1'')$$

These equations are specific for the thermodynamic evolutions:

• Isothermic ($T_2 = T_1 \Rightarrow i_2 = i_1$) $s_2 = s_1 - R\ln\frac{p_2}{p_1}$; $\left(inverse\ p_2 = p_1\exp^{-\frac{s_2-s_1}{R}}\right)$ (2)

• Isobaric ($p_2 = p_1$) $s_2 - s_1 = c_p\ln\frac{i_2}{i_1} \Rightarrow \frac{s_2-s_1}{c_p} = \ln\frac{i_2}{i_1} \;/\cdot\exp \Rightarrow \exp^{\frac{s_2-s_1}{c_p}} = \exp^{\ln\frac{i_2}{i_1}} \Rightarrow \exp^{\frac{s_2-s_1}{c_p}} = \frac{i_2}{i_1} \Rightarrow i_2 = i_1\exp^{\frac{s_2-s_1}{c_p}}$

$\left(inverse\ s_2 = s_1 + c_p\ln\frac{i_2}{i_1}\right)$ (3)

• Isentropic ($s_2 = s_1$) $c_p\ln\frac{i_2}{i_1} = R\ln\frac{p_2}{p_1} \Rightarrow \ln\frac{i_2}{i_1} = \ln\left(\frac{p_2}{p_1}\right)^{\frac{R}{c_p}} \Rightarrow i_2 = i_1\left(\frac{p_2}{p_1}\right)^{\frac{R}{c_p}} \Rightarrow i_2 = i_1\left(\frac{p_2}{p_1}\right)^{\frac{k-1}{k}}$ $\left(inverse\ p_2 = p_1\left(\frac{i_2}{i_1}\right)^{\frac{k}{k-1}}\right)$ (4)

In these relations, I approximate, according to [9, 11], c_p=1083.2 J/kgK, k=1.3623, as constants with temperature (R=288.1 J/kgK being a constant with temperature and having the same value for air and combustion gases). For kerosene (Jet-A1) I have minL=14.598 kg Air/kg Kerosene, the stoichiometric quantity of air to burn chemically complete the fuel, the chemical energy of the fuel E_0=43150 kJ/kg, according to [9, 13] and Wikipedia. With these data I will have a maximum enthalpy increase after combustion, with an excess air supply λ=1:

$$\Delta i = E_0/(\text{minL Kerosene}) = 43150/14.598 = 2955.9 \text{ kJ/kg}$$

The value corresponds, according with [9, 13] for the adiabatic combustion temperature of kerosene under ISA-International Standard Atmosphere conditions which is 2455^0C / 2730K.

I will consider the possibility of using hydrogen as fuel, with a major consequence in reducing the carbon footprint and protecting the ozone layer at the tropopause altitude. While the development of aviation combustion chambers using pure hydrogen fuel—rather than mixtures with methane as discussed in [35, 36]—is still under academic and experimental investigation, the thermodynamic parameters can be estimated using established combustion models [14, 37]. Although detailed specifications for aircraft-level hydrogen storage and delivery systems remain proprietary or in early development stages, current research on cryogenic storage and hydrogen aviation timelines (e.g., studies by Airbus and NASA) suggests such technologies will be available in the near future, validating the thermodynamic assumptions of this work.

Related to this topic, I present below a variant for calculating the hydrogen combustion parameters, according to [6, 7, 9, 10, 35, 36, 37] as follows. The combustion reaction of H_2 (above I wrote the relative atomic masses of the components to the atomic mass of hydrogen which is considered to have an atomic mass equal to 1), will be:

$$\overset{(1)}{\widetilde{2H_2}} + \overset{(16)}{\widetilde{O_2}} = \overset{(18)}{\widetilde{2H_2O}}$$

$$\text{so: } 4\text{kgH}_2 + 32\text{kgO}_2 = 36\text{kgH}_2\text{O} \;/:4$$

$$1\text{kgH}_2 + 8\text{kgO}_2 = 9\text{kgH}_2\text{O}$$

But 8 kg of O_2 it is found in 8•4,292 kg of air, therefor:

1kgH_2 burn with minL=8•4,292 kgL=34,336 kgL/kgH_2

So: minL=34,336 kg Air/kg Hydrogen

From [12] we have for hydrogen, approximately, E0=120000 kJ/kg, which results in an energy released after combustion, found in the enthalpy increase, of:

$$\Delta i = E_0/\text{minL } H_2 = 120000/34.336 = 3494.9 \text{ kJ/kg}$$

The approximation k=1.3623, is also verified by taking into account the tables for the values of absolute temperature T, specific enthalpy i and specific entropy s for air at the standard pressure of 101325 Pa, as well as other information from [8] and [10].

I calculated the ideal cycle parameters in the variants and sub-variants presented above, in the first phase, under ISA-International Standard Atmosphere conditions, at sea level (MSL-Mean Sea Level or H=0 m) and at speed v=0 (at a fixed point, Table 1) and for altitude H=8000m and

speed M=0.8 (i.e. v=246.4m/s, Table 2). The calculations were performed with 5 significant digits. I started from ISA conditions at sea level, i.e. p_0=101325 Pa and t_0=15^{0}C=288.2K, with i_0=312.2 kJ/kg and s_0=6.8349 kJ/kgK, as average values between air and burnt gases, according to [10].

For the classic Coanda-type jet variant, I used a TAE Centurion 125-02-99 engine, with the following parameters (according to TCDS EASA E.055 of Continental Aerospace Technologies GmbH and POH Diamond DA40 D of Diamond Aircraft Industries GmbH):

- Maximum take-off power: 100kW/135HP;
- Jet-A1 fuel consumption, at take-off power: 29.1 l/h=23.4 kg/h.

For the electro-jet engine type I will use an axial compressor of PT6A turboprop jet engine [28] driven by a high-speed electric motor MGV950CAX type (source www.parker.com) with a power of 170kW and a speed of 20,000 rpm (the MGV860CBD type with a power of 94kW and the same speed could also be used), a motor produced by Parker Hannifin Manufacturing France SAS, a branch of the AC890 Drive Association. To generate electricity, I will use Seebeck bridges TEG2-50-50-40/200 type (source www.eureca.de), which produce 40W of energy each, have dimensions of 50x50 mm, weigh 38 grams and are produced by EURECA Messtechnik GmbH (2500 pcs. with a mass of 95 kg and a surface area of 6.25 m^2 for which a length of the hot part, at take-off thrust conditions, would result in a first approximation of 2200 mm; the combustion chamber and the diffuser being annular in shape with an outer diameter of 500 mm and an inner diameter of 400 mm). If the onboard batteries are used as an additional source of electrical energy for takeoff and climb to cruising altitude, then the electrical energy generation area can be reduced to half the estimated length, i.e. 1100 mm, and, accordingly, the mass of the Seebeck bridges is reduced to 48 kg. It is observed, in the case of the electro-jet engine, that there is an isobaric evolution 3*- 4*, where a quantity of energy is spent, which represents the energy that is recovered, with the Seebeck bridges, from the gas flow after the combustion chamber. This gas energy is directly converted into electrical energy, part of this energy is used for the electric motor that drives the compressor and the surplus energy is stored in an on-board battery (in case there is a deficit of electrical energy, for example, during the take-off, initial climb and cruising climb to cruising altitude, part of the energy stored in the on-board batteries can be used). Generally, when cruising, the aircraft reduces its power, depending on the chosen cruise, between 45% and 75% (usually it is reduced to approximately 50%), so the necessary power generated by the Seebeck bridges, taking into account the dynamic compression due to the cruising speed, is generally below 50% of the maximum power required for takeoff and climb to the cruising altitude. In the case of converting the electro-jet into a ramjet, at the cruising speed and altitude, the electric generators are used as on-board generators, which supply the aircraft's electrical system and also recharge the on-board batteries. It should be noted that a rigorous system-level power density (thrust-to-weight ratio) comparison of the entire electro-jet propulsion train (including the high-capacity batteries, electric motor, and Seebeck bridges) against a standard turbocompressor unit is highly dependent on the development of aerospace-grade components. The current weight estimates (e.g., 48 to 95 kg for the Seebeck bridges) are based on commercial-off-the-shelf (COTS) thermoelectric modules, which are not optimized for aviation power-to-weight ratios. In a fully realized aviation-grade system, lightweight high-performance thermoelectric materials (such as optimized half-Heusler or oxyselenide alloys) would be used, significantly reducing the deadweight penalty. Furthermore, at cruise speeds where the electro-jet functions primarily as a ramjet, the shaft-less architecture avoids the weight of a standard turbocompressor, and the thermoelectric system's role transitions from primary motor driving to supplying auxiliary on-board systems and battery recharging, mitigating the weight penalty of the electrical conversion system during the main flight phase.

I present the calculation results for a 2-stage centrifugal compressor, classic turbojet (TR figured) and Coanda-type jet, with the two sub-variants, classic Coanda jet (CC figured) and electro-jet (CR figured), which will have the following parameters (the power corresponding to the calculated air flow is P=100kW):

$$\pi_c^* = 9{,}0;\ l_c^* = i_0\left(\pi_c^{*\frac{k-1}{k}} - 1\right) = 247{,}8 \text{ kJ/kg} \Rightarrow \dot{m}_a = \frac{P}{l_c^*} = 0{,}40355 \text{ kg/s};$$

The calculation was made both for kerosene (Jet-A1, with the extension -K) and hydrogen (H_2, with the extension -H) fuel variants as well.

Table 1. Jet engine parameters at H=0 m, v=0 m/s

PARAM.	p [Pa]	T [K]	i [kJ/kg]	s [kJ/kgK]	Tsp [m/s]	Csp [kg/Nh]	Δ % Tsp	Δ % Csp
0=1*	101325	288.2	312.2	6.8349				
2*	911925	517.0	560.0	6.8349				
3* TR	911925	2100.0	2274.7	8.3532				
4* TR	591015	1871.2	2026.9	8.3532				
5 TR-K	101325	1170.6	1268.0	8.3532	1283.7	0.11765		
5 TR-H	101325	1170.6	1268.0	8.3532	1249.9	0.04195		
Dif.TR-K/H							**-2.6**	**-64.3**
3* CC/R-K	911925	3245.8	3515.9	8.8248				
3* CC/R-H	911925	3743.4	4054.9	8.9793				
5 CC-K	101325	1809.4	1959.9	8.8248	1884.9	0.13083	**46.8**	**11.2**
5 CC-H	101325	2086.7	2260.3	8.9793	1949.6	0.05378	**56.0**	**28.2**
Dif.CC-K/H							**3.4**	**-58.9**
4* CR-K	911925	2998.8	3268.1	8.7457				
4* CR-H	911925	3514.7	3807.1	8.9110				
5 CR-K	101325	1681.9	1821.8	8.7457	1817.3	0.13570	**41.6**	**15.3**
5 CR-H	101325	1959.2	2122.2	8.9110	1889.1	0.05550	**51.1**	**32.3**
Dif.CR-K/H							**4.0**	**-59.1**

Table 2. Jet engine parameters at H=8000 m, v=246.4 m/s

PARAM.	p [Pa]	T [K]	i [kJ/kg]	s [kJ/kgK]	Tsp [m/s]	Csp [kg/Nh]	Δ % Tsp	Δ % Csp
H	35650	236.1	255.7	6.9199				
1*	54352	264.1	286.1	6.9199				
2*	489182	473.8	513.2	6.9199				
3* TR	489182	2100.0	2274.7	8.5326				
4* TR	329385	1890.3	2047.6	8.5326				
5 TR-K	35650	1046.4	1133.5	8.5326	1164.0	0.13328		
5 TR-H	35650	1046.4	1133.5	8.5326	1126.0	0.04784		
Dif.TR-K/H							**-3.3**	**-64.1**
3* CC/R-K	489182	3202.6	3469.1	8.9898				
3* CC/R-H	489182	3700.2	4008.1	9.1462				
5 CC-K	35650	1595.9	1728.7	8.9898	1747.1	0.14115	**50.1**	**5.9**
5 CC-H	35650	1843.8	1997.2	9.1462	1817.4	0.05769	**61.4**	**20.6**
Dif.CC-K/H							**4.0**	**-59.2**
4* CR-K	489182	2993.0	3242.0	8.9164				
4* CR-H	489182	3490.6	3781.0	9.0830				
5 CR-K	35650	1491.4	1615.5	8.9164	1680.8	0.14672	**44.4**	**10.1**
5 CR-H	35650	1739.4	1884.1	9.0830	1758.1	0.05964	**56.1**	**24.7**
Dif.CR-K/H							**4.6**	**-59.3**

With these calculated data, the i-s diagrams are drawn for the three variants with one, respectively, with two sub-variants (I mention that these variants were drawn to scale, Figures 2, 3 and 4):

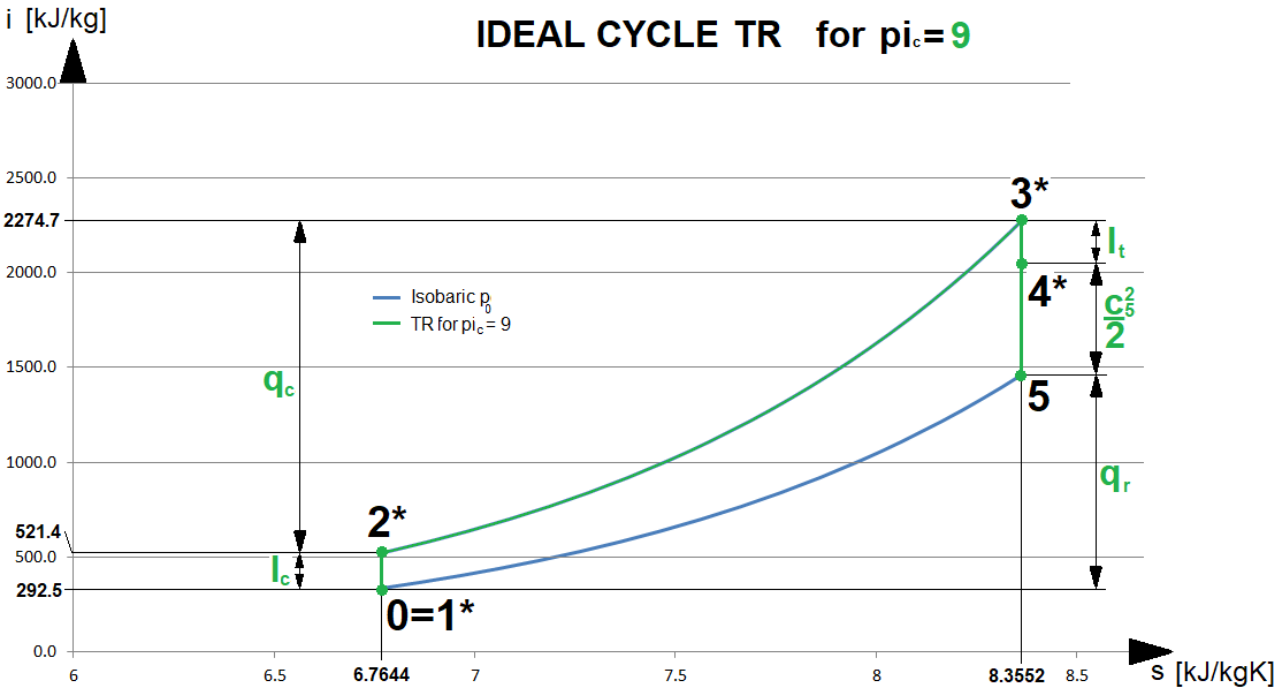

Figure 2. Ideal cycle for turbo-jet engine

In the case of the Coanda-type jet, in the classical and electric versions the relationship between the mechanical compression work l_c and the power P of the piston engine or electric motor is: $P=l_c \cdot \dot{m}_a$, where $\dot{m}_a$ is the air flow of the compressor.

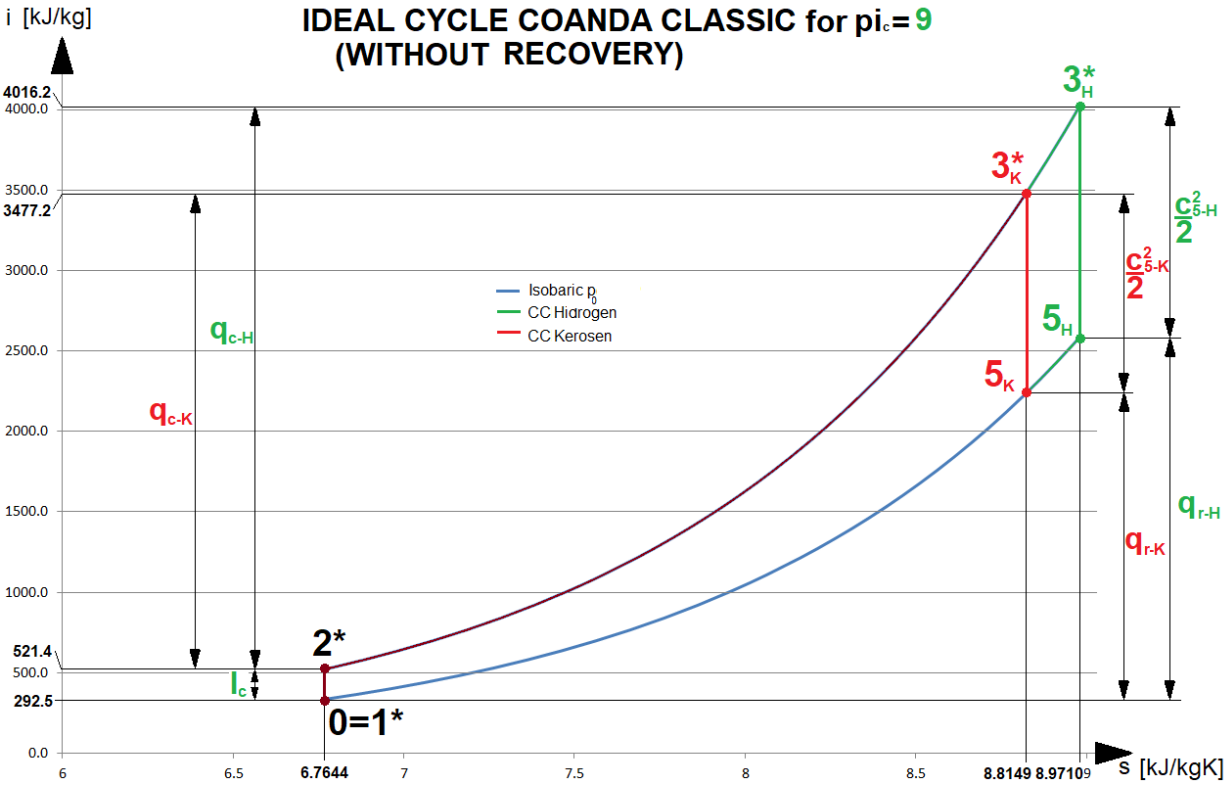

Figure 3. Ideal cycle for Coanda-type jet engine

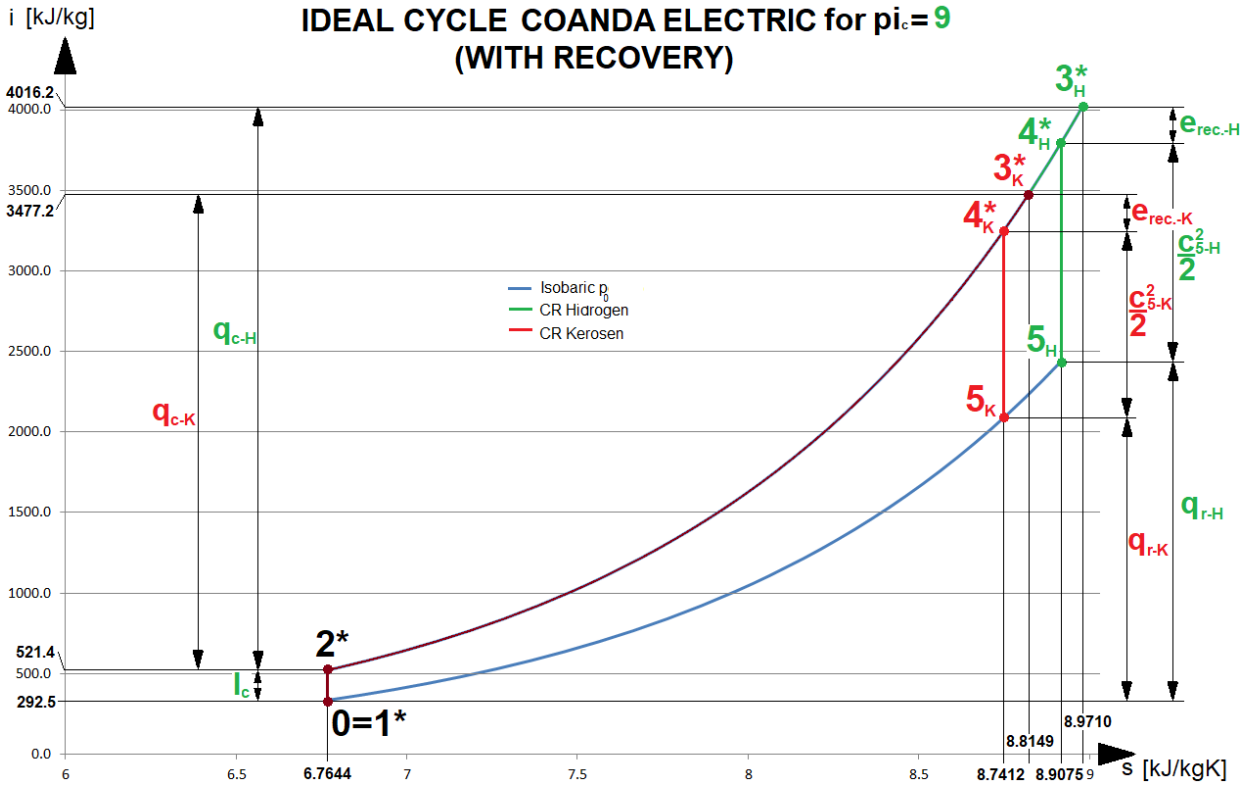

Figure 4. Ideal cycle for electro-jet engine (recovery jet engine)

To be closer to reality, I will also do a check in the real cycle, for MSL and fixed-point variants, and for the calculation of the real cycle I will use the thermodynamic tables from [10] but also information about the thermodynamic parameters of some combustible substances, such as kerosene and hydrogen, from [6] and [8]. I will also consider the dissociation during combustion for the first equilibrium.

Thus, for the calculation of the composition of the burnt gases in the case of kerosene (or Jet-A1 fuel), according to [10], I can consider a mass participation of the standard fuel (for simplification) as follows:

c=0.8608 kg C/kg fuel; h=0.1392 kg H/kg fuel,

and for a mass composition of air (considering, for simplification, that it has a volumetric composition of 79% N_2 and 21% O_2, where the percentage of approximately 1% Ar was added to nitrogen which is an inert gas, and the rest of the components, which are below 0.1%, will be neglected) of approximately (we symbolize air with L):

4.292 kg L/kg O2 (and, respectively, 3.292 kg N2/kg O2)

In this case, I have:

minL kg=4.292(8/3c + 8h) kg L/kg fuel=14.632 kg L/kg fuel for stoichiometric conditions

If kerosene is considered as a hydrocarbon compound with a conventional chemical formula of the form $C_{12}H_{23}$ as defined in [14], from which a mass participation results as:

c=0.8623 kg C/kg fuel; h=0.1377 kg H/kg fuel, which results in a value minL=14.598 kg L/kg fuel, values that are close to the values above and I will use in the future.

For the calculation of the combustion temperature, information from [6, 8] and [10] will be used, as follows:

- the energy balance of the combustion will be, according to [8]:

$$\dot{m}_c i_{comb.\text{-}Tini.} + \dot{m}_a i_{aer\text{-}Tini.} + \dot{m}_c E_0 = \dot{m}_g i_{g.a.\text{-}Tini.} + \dot{m}_c (Q_p)_{Tini.} = \dot{m}_g i_{g.a.\text{-}Tfin.} \text{ where:}$$

$$\dot{m}_a/\dot{m}_c = \lambda minL \text{ si } \dot{m}_g = \dot{m}_a + \dot{m}_c \text{ and I have:}$$

$$i_{comb.\text{-}Tini.} + \lambda minL\, i_{aer\text{-}Tini.} + E_0 = (1+\lambda minL) i_{g.a.\text{-}Tini.} + (Q_p)_{Tini.} = (1+\lambda minL) i_{g.a.\text{-}Tfin.}$$

where:

- i is the enthalpy of the fuel, air or burnt gases at the initial and final temperatures, respectively;
- E_0 is the chemical energy of the fuel (sometimes it can be defined as the lower or upper calorific value Pci or Pcs);
- $(Q_p)T$ is the heat of reaction, at constant pressure, and at a certain temperature.

These last two quantities can be taken from thermodynamic tables, or can be calculated approximately, according to [8]:

$(Q_p)_{C\alpha H\beta\text{-}T} \approx 393777\alpha + 241989(\beta/2)$ kJ/kmol and:

$P_{ci} \approx 32814c + 120995h$ kJ/kg.

If the enthalpy of the initial substances is considered to be $i_{s.i.\text{-}Tini.} = i_{comb.\text{-}Tini.} + \lambda \min L i_{aer\text{-}Tini.}$ and the enthalpy of the final substances $i_{s.f.\text{-}T} = (1+\lambda \min L) i_{g.a.\text{-}T}$ at the initial and final temperatures, respectively, the energy balance will become (in all these cases the heat of formation of the component substances is neglected):

$$i_{s.i.\text{-}Tini.} + E_0 = i_{s.f.\text{-}Tini.} + (Q_p)_{Tini.} = i_{s.f.\text{-}Tfin.}$$

where I have, formally, two evolutions (equivalent to the chemical reaction of fuel combustion), respectively, a first transformation of isothermal input of chemical energy of the fuel E_0 at temperature $T_{ini.}$, followed by a transformation of isobaric input of reaction energy at constant pressure Q_p, between the initial temperature $T_{ini.}$ and the final temperature $T_{fin.}$.

I will consider the values for these quantities, for kerosene, from tables in [6, 8] and [10] as follows:

$E_0 = 43150$ kJ/kg, $(Q_p)_{500K} = 7039050$ kJ/kmol.

In the case of hydrogen, I mention again that I did not found sufficient documentation for the combustion parameters, finding only the following data presented by Alejandro Millán-Merino and Pierre Boivin [14]:

- according to [11] $(Q_p)_{500K} = 243642$ kJ/kmol si $(Q_p)_{550K} = 244111$ kJ/kmol;
- according to [7] $P_{ci} = 119617$ kJ/kg, $P_{cs} = 141974$ kJ/kg = 242071 kJ/kmol,

$Q_p = 241746$ kJ/kmol = 119910 kJ/kg (water vapor, T not defined),

$Q_p = 285791$ kJ/kmol = 59491 kJ/kg (liquid water, T not defined),

$R = 412$ J/kgK, $\mu = 2{,}016$ kg/kmol, $\min O_2 = 8$ kg O_2/kg H_2,

$\min L = 34{,}336$ kgL/kg H_2.

I will consider $E_0 = 120000$ kJ/kg, $(Q_p)_{500K} = 238642$ kJ/kmol si $(Q_p)_{550K} = 240111$ kJ/kmol, $R = 412$ J/kgK, $\mu = 2{,}016$ kg/kmol that is the kmol mass, $\min L = 34{,}336$ kgL/kg H_2.

For a most accurate calculation of the combustion temperature, I will also consider the dissociation reactions, taking into account the first dissociation equilibrium, both for kerosene and for hydrogen. According to [8] and [10], in the case of dissociation, I have an equilibrium for the components before and after dissociation, of the form:

$$qA + rB + \ldots \leftrightarrow sC + tD + \ldots$$

where: $\overrightarrow{W_1} = k_1 \bullet p_A^q \bullet \ p_B^r \bullet \ldots$ is the reaction speed of the initial gas substances, that has p_A, p_B, ... are partial pressure for initial gases, and $\overleftarrow{W_2} = k_2 \bullet p_C^s \bullet \ p_D^t \bullet \ldots$ is the reaction speed of the final gas substances, that has p_C, p_D, ... are partial pressure for initial gases, and $\overrightarrow{W_1} = \overleftarrow{W_2}$, where k_1 and k_2 are the reaction constants.

The equilibrium equation can be written in the form:

$$K_p = \frac{k_1}{k_2} = \frac{p_C^s \bullet \ p_D^t \bullet \ldots}{p_A^q \bullet \ p_B^r \bullet \ldots}$$

where K_p is an equilibrium constant.

From the properties of the gas mixture, according to [10] we have:

$p_{am} = \sum_{i=1}^{n} p_i$, where $p_i = r_i p_{am}$, where $r_i = V_i/V$ is the volume participation of gases in the mixture, and p_i is the partial pressure of gases in the mixture, and:

$$V = \sum_{i=1}^{n} V_i \, , \ \sum_{i=1}^{n} r_i = 1$$

and

$$r_i = \frac{\frac{m_i}{\mu_i}}{\sum_{i=1}^{n} \frac{m_i}{\mu_i}} = \frac{\nu_i}{\nu_{am}}$$

where $\nu_{am} = \sum_{i=1}^{n} \frac{m_i}{\mu_i}$, ν_i is the kmol quantity of i component, and μ_i is the kmol mass of i component.

From here we have:

$$p_i = \frac{\nu_i}{\nu_{am}} \, p_{am}$$

Under these conditions, I will have:

$$K_p = \left(\frac{p_{am}}{\nu_{am}}\right)^{(s+t+\ldots)-(q+r+\ldots)} \frac{\nu_C^s \bullet \nu_D^t \bullet \ldots}{\nu_A^q \bullet \nu_B^r \bullet \ldots}$$

I will consider the first equilibrium, which is as follows:

- for kerosene: carbon monoxide equilibrium: $CO + 1/2O_2 \leftrightarrow CO_2$;
- for hydrogen: hydrogen equilibrium [14]: $H_2 + 1/2O_2 \leftrightarrow H_2O$.

From an energetic point of view, in the case of considering dissociations, the energy balance is:

$$i_{s.i.\text{-}Tini.} + E_0 = i_{s.f.\text{-}Tini.} + (Q_p)_{Tini.} = i_{s.f.\text{-}Tfin.\text{-}disoc.} + E_{0\text{-}disoc}$$

where: $E_{0\text{-}disoc.}$ is the energy lost due to dissociation reactions that will be subtracted from the enthalpy of the final substances at the final temperature $i_{s.f.\text{-}Tfin.} = i_{s.f.\text{-}Tfin.\text{-}disoc.} + E_{0\text{-}disoc.}$, which means a decrease in enthalpy, respectively a decrease of the final temperature after combustion.

To estimate the losses in the jet engine, I took information from [8] and [13], as follows:

- $\sigma_{DA}^{*} = 0,98$ total pressure losses in the intake device;
- $\eta_{C}^{*} = 0,75$ compressor efficiency;
- $\sigma_{CA}^{*} = 0,95$ total pressure losses in the combustion chamber;
- $\xi_{CA} = 0,95$ combustion chamber perfection coefficient;
- $\eta_{T}^{*} = 0,90$ turbine efficiency;
- $\eta_{M} = 0,99$ mechanical efficiency;
- $\varphi_{AR} = 0,97$ losses in the jet nozzle.

The calculation of the real cycles was made for ISA conditions ($T_0 = 288.16K$, $p_0 = 101325Pa$), at H = 0m and v = 0m/s. The calculations were made using the thermodynamic tables from [10]. Kerosene (Jet A1 fuel) will be taken into account defined as the approximate chemical formula $C_{12}H_{23}$, according to [13] (Table 3). The interpolations between the intermediate values in the tables are linear interpolations. I will consider $R_{air} = 0.2882$ kJ / kgK, $k_{air\text{-}average} = 1.39$ (constant between 300K and 550K). I chose $\pi_{c}^{*} = 9.00$ and, for TR (classic turbojet), T3 * = 2100K. For Coanda-type jets, both variants, classic and electric, I consider $\lambda = 1.05$, taking into account the secondary flow through the combustion chamber to protect its walls. Calculations were made with 5 significant digits with rounding.

Table 3. Real cycle parameters for jet engines

Param.	**p**	**T**	**i**	**s**	**Tsp**	**Csp**	**lc***
↓POINT	[Pa]	[K]	[kJ/kg]	[kJ/kgK]	[m/s]	[kg/Nh]	[kJ/kg]
0	101325	288.2	287.1	6.8210	-	-	-
1*	99299	288.2	287.1	6.8268	-	-	-
2*id	893687	540.0	537.9	6.8268	-	-	250.77
2*	893687	584.3	582.1	6.8486	-	-	295.02
3* TR-K	849003	2100.0	2567.5	8.4594	-	-	-
4* TR-Kid	471482	1826.4	2236.4	8.4594	-	-	-
4* TR-K	471482	1850.0	2269.5	8.4776	-	-	-
5 TR-Kid	101325	1322.1	1544.1	8.4776	1204.5	-	-
5 TR-K	101325	1379.0	1586.9	8.4982	1224.9	0.1422	-
3* TR-H	849003	2100.0	2815.1	9.2581	-	-	-
4* TR-Hid	504603	1882.8	2484.0	9.2581	-	-	-
4* TR-H	504603	1904.7	2517.1	9.2763	-	-	-
5 TR-Hid	101325	1344.8	1692.1	9.2763	1284.5	-	-
5 TR-H	101325	1379.8	1740.8	9.3076	1268.5	0.0513	-
3* CC/R-K	849003	2504.2	3133.7	8.7060	-	-	-
5 CC-Kid	101325	1607.7	1894.3	8.7060	1574.4	-	-
5 CC-K	101325	1459.3	1967.5	9.8970	1626.8	0.1444	-
3* CC/R-H	849003	2645.5	3963.7	10.1443	-	-	-
5 CC-Hid	101325	1729.3	2422.3	10.1443	1755.8	-	-
5 CC-H	101325	1789.0	2513.4	10.1738	1750.3	0.0570	**e-rec***
4* CR-K	849003	2239.1	2761.2	8.5487	-	-	372.5
5 CR-Kid	101325	1428.7	1655.9	8.5487	1486.8	-	-
5 CR-K	101325	1297.8	1721.2	9.7178	1536.3	0.1529	-
4* CR-H	849003	2428.9	3591.2	9.9970	-	-	372.5
5 CR-Hid	101325	1578.0	2179.1	9.9970	1680.5	-	-
5 CR-H	101325	1633.6	2262.6	10.0270	1675.3	0.0596	-

4 Conclusions

As a conclusion of the comparative theoretical study, on ideal cycle, for various heights and speeds, and between the ideal cycle and the real cycle on the ground and at a fixed point, it results:

- on the ground and at a fixed point, the electro-jet engine has an increase of 41.6% in specific thrust compared to the Whittle-type turbo-jet engine, with an increase in specific fuel consumption of 15.3% if kerosene is used as fuel, and an increase of 51.1% in thrust and of 32.3% in specific fuel consumption if hydrogen is used as fuel;

- at 8000 m and at M 0.8 (246.4 m/s = 887 km/h = 479 kts) the increase in specific thrust of the electro-jet engine is 44.4% with an increase of the specific fuel consumption of 10.1% compared to the Whittle-type turbo-jet engine if kerosene is used as fuel, and a 56.1% increase in specific thrust with a 24.1% increase in specific fuel consumption, if hydrogen is used as fuel. This estimation was made on the ideal cycle for both jet engine variants.

For the calculation on the real cycle, taking into account the first equilibrium for the combustion with dissociation, on the ground and at a fixed point, the increase in thrust for the electro-jet engine, compared to the turbo-jet engine is of 25.4% for the specific thrust and of 7.5% for the specific fuel consumption, when using kerosene as fuel and of 32.1% for the specific thrust and a 16.2% increase in the specific fuel consumption, when using hydrogen as fuel.

I mention that I made this calculation taking into account the recovery of thermal energy from the main flow of exhaust gases for the generation of electrical energy with Seebeck bridges. I mention that in chapter 8, I make an experimental estimation of the recovery of the energy lost through the hot parts of a small turbo-shaft jet engine, energy that constitutes an irretrievable loss in a conventional turbojet.

5 Types of Thermo-Electric Generators That Could Be Used for Electro-Jet Engine

I will present, without limiting myself to these, several types of thermoelectric generators that could be used to convert thermal energy in the form of heat directly into electrical energy, according to [15].

5.1 Thermo-electronic generator

A thermo-electronic generator is based on the emission of electrons from a cathode heated to a sufficiently high temperature to set the conduction electrons in motion. Such a generator is based on Richardson's theory of electron emission (Figure 5).

The Richardson formula is:

$$j = BT^2 \exp^{-\frac{\varphi}{kT}}$$

where:

j → current density in A/cm^2;
B → a constant = 120 A/(cm^{2}K^2);
T → absolute temperature in K;
φ → work of extraction of the electron in eV;
k → Boltzmann constant = 8,62·10^{-5} eV/K.

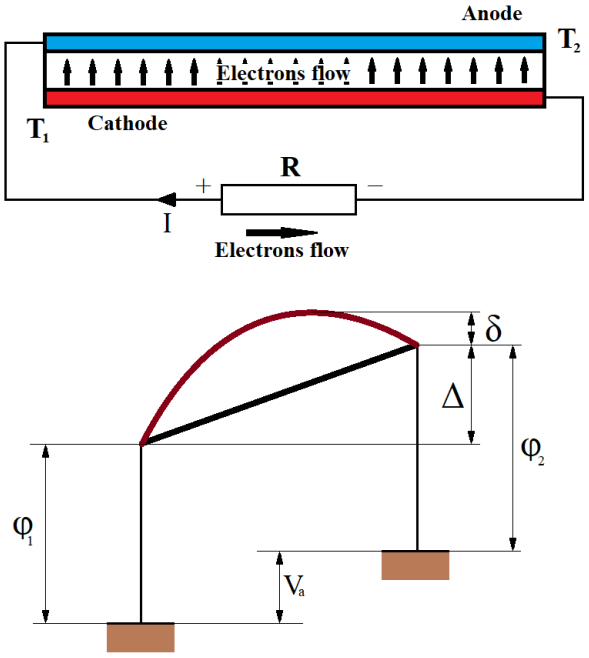

Figure 5. Thermo-electronic generator layout and energy levels of the generator

The thermo-electronic generator could be used in the combustion chamber area, when using materials that can withstand high temperatures, such as tungsten (or wolfram). The technical condition that determines the use of this method is the very small gap between the anode and cathode, the electrodes generating electro-motor voltage, of the order of tenths or hundredths of a millimeter, but also maintaining the vacuum between the anode and cathode that is a technical difficulty.

5.2 Magneto-hydro-dynamic (mhd) generator

The Magneto-hydro-dynamic generator is based on the Lorentz theory, in such a sense that in a magnetic field $\boldsymbol{B}$, in which an ionized gas moves with a velocity $\boldsymbol{v}$, an electromotive force (E.M.F.) $\boldsymbol{E}$ is generated between two plates connected to a load resistance R_{load} (Figure 6).

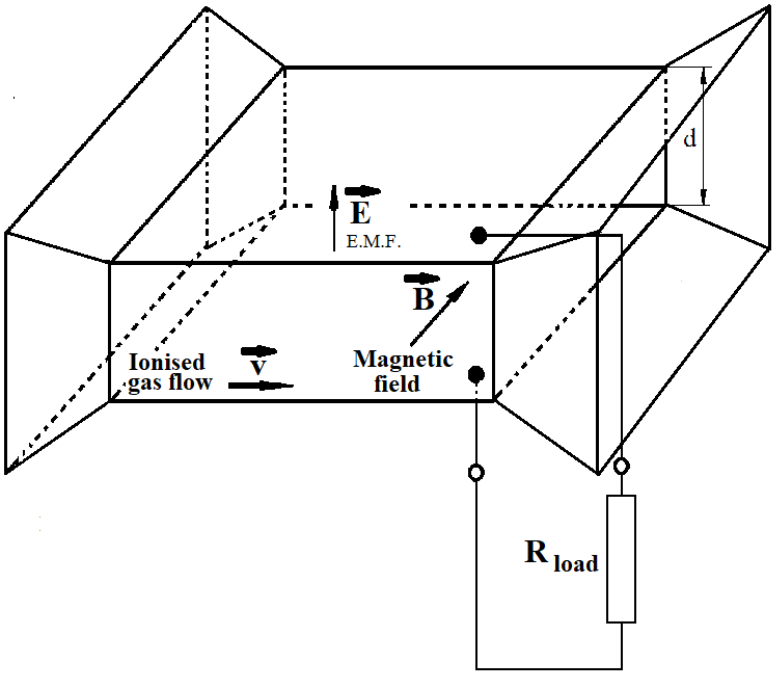

Figure 6. Magneto-hydro-dynamic generator layout

According to Lorentz's theory, the force generated by the electric charge q moving with a velocity $\boldsymbol{v}$ in the magnetic field of intensity $\boldsymbol{B}$ is:

$$\boldsymbol{F}_{Lorentz} = q(\boldsymbol{v}\text{x}\boldsymbol{B})$$

In this first case, the Lorentz force is

$$\boldsymbol{F} = q(\boldsymbol{E}+\boldsymbol{v}\text{x}\boldsymbol{B})$$

where $\boldsymbol{E}$ is the electric field existing in the working gas flow area (Figure 7).

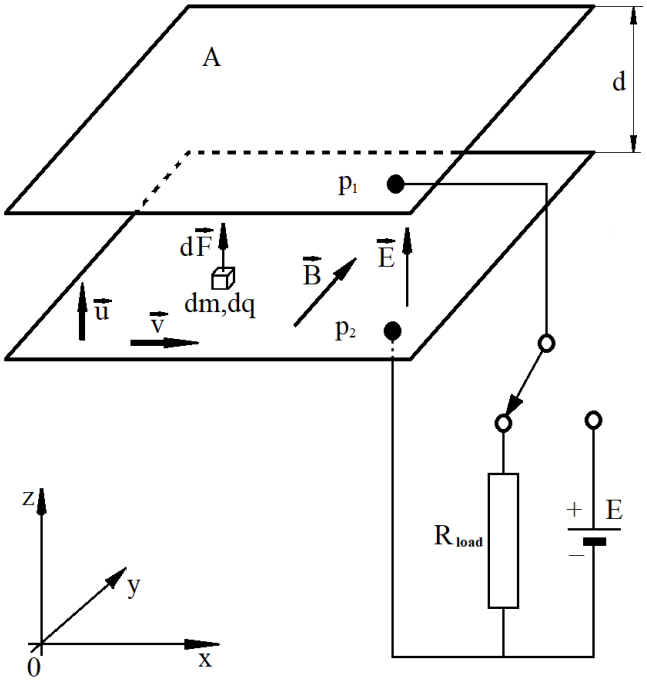

Figure 7. Magneto-hydro-dynamic generator equilibrium

But because of the electric field $\boldsymbol{E}$ generated by the electric potential difference U between plates p_1 and p_2, an electromagnetic force appears that causes the ionized working gas particle move at velocity $\boldsymbol{u}$, from p_2 to p_1.

So, finally, the force $\boldsymbol{F}$ acting on the ionized working gas particle, moving in the generation zone (between plates p_1 and p_2) is:

$$\boldsymbol{F} = q(\boldsymbol{E} + \boldsymbol{v}\text{x}\boldsymbol{B} + \boldsymbol{u}\text{x}\boldsymbol{B})$$

where $\boldsymbol{u}$ is the velocity of movement of the particle from plate p_2 to plate p_1, and:
$E = \frac{U}{d}$, where U is the potential difference between plates p_1 and p_2 and d is the distance between them.
In this case:

$$U_{total} = U + B \cdot v$$

where $B \cdot v = U_0$ is the open-circuit e.m.f. (considering also that vectors $\boldsymbol{v}$ and $\boldsymbol{u}$ are perpendicular to vector $\boldsymbol{B}$).

The magneto-hydro-dynamic generator would be suitable for use, but due to the need to use a strong magnetic field (which can be generated by powerful electromagnets, which are heavy and require high electrical power) and the need to ionize the exhaust gases, which is done by spraying ionizing elements (such as potassium or cesium powder) which would be a polluting and very expensive material, it is not feasible for use in aviation for this type of jet engine.

5.3 Seebeck thermo-electric generator (teg)

The Seebeck thermoelectric generator is based on the appearance of a potential difference between two conductors of different materials welded together. This phenomenon is called the thermoelectric effect or Seebeck effect.

The generator is composed of two welds between two such materials, one of the welds being placed in the hot source and the other being placed in the cold source (Figure 8).

The Seebeck electromotive force, as a potential difference is: $\Delta E = \alpha \Delta T / \cdot d \Rightarrow dE = \alpha dT, \{E_1 - E_2 = \alpha(T_1 - T_2)\}$

The coefficient α, in some books is called the thermal force and is measured in [V/K].

The energy transformed from the form of heat is: $Q = \Phi \cdot I \cdot t$, where Φ is called the Peltier coefficient, $\Phi = \alpha T \Rightarrow Q = \alpha T I t$, t is time and where:

Received heat : $Q_1^{rec.} = \alpha T_1 I t$: from hot source;

Disposed heat : $Q_2^{dis.} = \alpha T_2 I t$: from cold source;

And work is : $L = \alpha(T_1 - T_2) I t = Q_1^{rec.} - Q_2^{dis.}$.

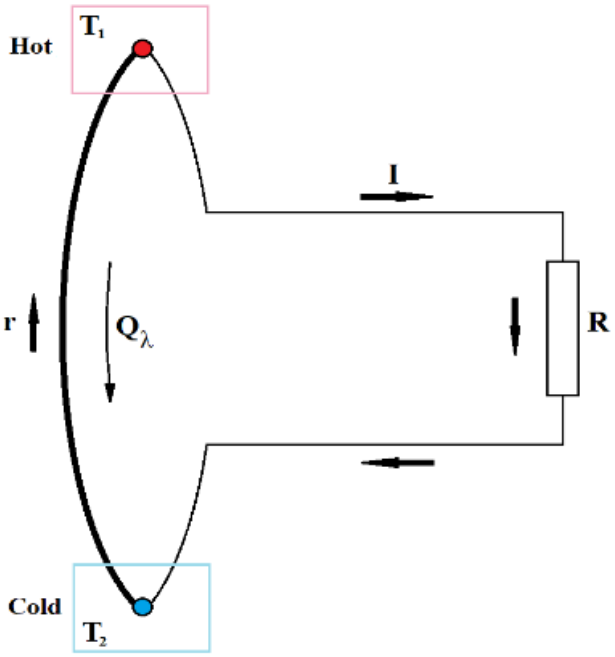

Figure 8. Seebeck generator layout

In this case the work L is:

$$L = Q_{Joule} + L_{cycle} = \alpha(T_1 - T_2) I t \Rightarrow L_{cycle} = \alpha(T_1 - T_2) I t - Q_{Joule} = I^2 R t$$

and the generated power is:

$$P = I^2 R = \alpha(T_1 - T_2) I$$

If $Q_\lambda^{conduction}$ is the heat exchanged by conduction between the hot source and the cold source, and Q_{Joule} is the heat released by the thermo-electric Joule effect, produced by the electric current circulating through the conductors, it is considered that this is divided into equal amounts for each source, that is, for each section of conductor.

So, in total, have:

$Q_1=Q_1^{rec.}+Q_\lambda^{conduction}$-$1/2Q_{Joule}$: from the hot source;

$Q_2=Q_2^{dis.}+Q_\lambda^{conduction}$+$1/2Q_{Joule}$: from the cold source;

and the efficiency of the TEG is:

$$\eta_t = \frac{L_{cycle}}{Q_1} = \frac{I^2Rt}{Q_1^{rec.}+Q_\lambda^{conduction}-\frac{1}{2}Q_{Joule}}$$

and if $Q_\lambda^{conduction}=0$ and $Q_{Joule}=0$ then $L_{cycle}=\alpha(T_1\text{-}T_2)It$, $Q_1=\alpha T_1 It$ and then:

$$\eta_t^{\text{Zero losses}} = \frac{L_{cycle}}{Q_1} = \frac{\alpha(T_1-T_2)It}{\alpha T_1 It} = \frac{T_1-T_2}{T_1} = 1-\frac{T_2}{T_1}$$

therefor that is the efficiency of a Carnot cycle, where T_2 is the temperature of the cold source and T_1 is the temperature of the hot source. This is the ideal situation in which the heat conduction and heat losses as Joule effect through the conductors are not taken into account.

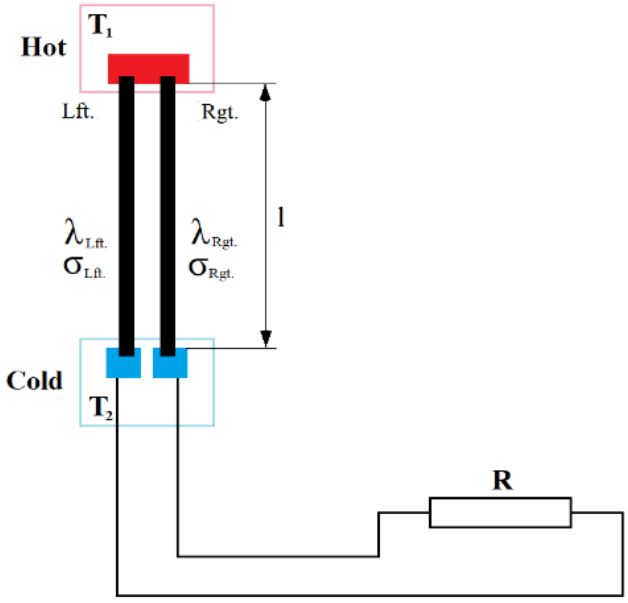

Figure 9. Seebeck element layout

If I take account of these losses, I will have:

$$P_\lambda^{conduction}t=Q_\lambda^{conduction}=\frac{\lambda_{lft.}\sigma_{lft.}-\lambda_{rgt.}\sigma_{rgt.}}{l}(T_1-T_2)\,t=\Psi(T_1-T_2)\,t$$

where $P_\lambda^{conduction}$, is the power transmitted through conduction, $\Psi=\frac{\lambda_{lft.}\sigma_{lft.}-\lambda_{rgt.}\sigma_{rgt.}}{l}$, and σ is the cross-section of the left and right side conductors and λ is the thermal conductivity of the left and right side conductors (Figure 9).

$$P_{Joule}t=Q_{Joule}=I^2rt$$

where $r=\left(\frac{\rho_{lft.}}{\sigma_{lft.}}+\frac{\rho_{rgt.}}{\sigma_{rgt.}}\right)l$, and P_{Joule} is the power lost as Joule effect, and ρ is the resistivity of the conductors on the left and right side. If $\gamma=\frac{R}{r}$, I will have:

$$I=\frac{\alpha(T_1-T_2)}{r+R}=\frac{\alpha(T_1-T_2)}{r(1+\gamma)};\ Q_1^{rec.}=\frac{\alpha^2T_1(T_1-T_2)t}{r(1+\gamma)};\ L_{cycle}=\frac{\alpha^2(T_1-T_2)^2\gamma t}{r(1+\gamma)^2};\ Q_{Joule}=\frac{\alpha^2(T_1-T_2)^2t}{r(1+\gamma)^2}$$

and then,

$$\eta_t=\frac{\frac{\alpha^2(T_1-T_2)^2\gamma t}{r(1+\gamma)^2}}{\frac{\alpha^2T_1(T_1-T_2)t}{r(1+\gamma)}+\Psi t(T_1-T_2)-\frac{1}{2}\frac{\alpha^2(T_1-T_2)^2t}{r(1+\gamma)^2}}=\frac{\frac{T_1-T_2}{T_1}}{1+\frac{\Psi r}{\alpha^2}\frac{(1+\gamma)^2}{T_1\gamma}+\frac{1}{2}\frac{T_1+T_2}{T_1\gamma}}=$$

$$\eta_t^{Carnot}\frac{1}{1+\frac{\Psi_r}{\alpha^2}\frac{(1+\gamma)^2}{T_1\gamma}+\frac{1}{2}\frac{T_1+T_2}{T_1\gamma}}$$

where: $z=\frac{\alpha^2}{\Psi_r}$ is A.F. Ioffe coefficient $z=\frac{\alpha^2}{\lambda_{lft.}\rho_{lft.}+\lambda_{rgt.}\rho_{rgt.}\frac{\sigma_{rgt.}}{\sigma_{lft.}}+\lambda_{lft.}\rho_{rgt.}\frac{\sigma_{lft.}}{\sigma_{rgt.}}+\lambda_{rgt.}\rho_{rgt.}}$, and:

η_t is maximum when z is maximum (or 1/z → is minimum) but z depends on α, $\lambda_{lft./rgt.}$ which are the thermal conductivity coefficients and $\rho_{lft./rgt.}$ the resistivity of the conductors but also on $\left(\frac{\sigma_{lft.}}{\sigma_{rgt.}}\right)$ the ratio of the conductor sections, that is:

$$z'\left(\frac{\sigma_{lft.}}{\sigma_{rgt.}}\right)=0 \text{ when } \left(\frac{\sigma_{lft.}}{\sigma_{rgt.}}\right)_{(for\ z=max.)}=\sqrt{\lambda_{rgt.}\frac{\lambda_{rgt.}\rho_{lft.}}{\lambda_{lft.}\rho_{rgt.}}} \text{ and}$$

$$z_{max.}=\left(\frac{\alpha}{\sqrt{\lambda_{lft.}\rho_{rgt.}}+\sqrt{\lambda_{lft.}\rho_{rgt.}}}\right)^2$$

and for $\lambda_{rgt.}=\lambda_{lft.}=\lambda$ and $\rho_{rgt.}=\rho_{lft.}=\rho$ thus

$$z_{max.}=\frac{\alpha^2}{4\lambda\rho} \tag{5}$$

Similar for η_t=maximum with respect to γ, denoted by $\gamma_{max.}$, where:

$$\gamma_{max.}=\sqrt{z\frac{T_1+T_2}{2}+1}\,, \tag{6}$$

and $\eta_t=\eta_t^{Carnot}\frac{1}{1+\frac{2(1+\gamma_{max.})}{zT_1}}$ or for z according to $\gamma_{max.}$ will have:

$$\eta_t=\eta_t^{Carnot}\frac{\gamma_{max.}-1}{\gamma_{max.}+\frac{T_2}{T_1}} \tag{7}$$

{and for $Q_{Joule}\approx 0$ I will have $\eta_t=\eta_t^{Carnot}\frac{\gamma'_{max.}-1}{\gamma'_{max.}+1}$ where $\gamma'_{max.}=\sqrt{1+z_{max.}T_1}$ }

If I make a comparative analysis of the three systems for converting thermal energy directly into electrical energy presented above, the conclusion drawn is that a Seebeck-type bridge thermoelectric converter is the best option, both from the point of view of costs and from the point of view of its applicability in aviation.

Thus, bridges with low operating temperatures, between 200^0C and 1000^0C, which are currently mass-produced, can be used. Even if these Seebeck bridges have low transfer efficiencies (between 5% and 30%), considering that they are used to recover heat that is lost by conduction through the walls of the jet engine to the outside, they can be used as a cooling and insulating option for these surfaces. For the heat exchange carried out in the gas flow after the combustion chamber, with the role of replacing the gas turbine, materials that allow high operating temperatures, from 1500^0C to 2500^0C, and with higher efficiencies, of about 30% are suitable. For this reason, I will present such materials, respectively, thermocouples material, in the next chapter.

6 Seebeck Materials [18, 19], [23–27], [30, 31, 33, 34]

For mass-produced Seebeck bridges, the materials used are semiconductor metals alloyed and doped to form p- or n-type junctions. The semiconductor materials can be used up to maximum temperatures of approximately 250^0C. These can use an alloy of Germanium and Silicon, the first types of such bridges manufactured. Other types of generators can use alloys of Bismuth, Antimony and Tellurium, such as $(BiSb)_2Te_3$ and $Bi_2(TeSe)_3$.

Germanium-Tellurium and Lead-Tellurium alloys can also be used. Newer research also uses other alloys, in which metals are used, as follows, but not limited to: Fe, Cs, Ca, Ce, Mn, Sn, Co, Ce, Ag, La, Nd, S, C, all of these alloys greatly improving the performance of these generators.

For high temperatures, typical for the gas temperature of jet engines of this type, combinations of Nickel, Chromium, Silicon, Magnesium, Aluminum, Manganese can be used for temperatures up to 1200^0C, Platinum-Rhodium alloys for temperatures between 1500^0C and 1700^0C and Tungsten (Wolfram)-Rhenium for temperatures above 2300^0C [20] basically used for pyrometer technology. These last thermocouples can be used to recover energy from the gas flow after the combustion chamber, but their thermoelectric figure of merit is extremely low, making them unsuitable for efficient power generation compared to pyrometry. For actual energy recovery, advanced thermoelectric materials with a higher figure of merit (ZT) are required. For example, oxyselenides (BiCuSeO) can achieve a ZT of approximately 1.4 at 800 K, and SnSeS compounds have been reported to reach a ZT of 3.07 at 700 K [30], while radioisotope thermoelectric generator materials can operate up to 1200 K. However, due to high costs and material limitations, metal-based high-temperature thermocouples remain restricted to pyrometer technology or specialized space applications. Recent research has used oxide-based materials for such generators, with operating temperatures comparable to those of high-melting-point metals.

7 Current cases of thermoelectric converters use

Apart from the use in ground heat recovery installations, in thermoelectric power plants or industrial installations that release residual substance at high temperature, in which case magneto-hydro-dynamic generators can be used with good efficiency, I have found such systems, mainly Seebeck-type thermoelectric systems in the automotive sector [29, 32].

These systems recover between 330W and 1000W on automobile, reaching values of 3000W to 5000W on truck train and vessel engines. The efficiencies of these systems, due to the lower operating temperatures, are between 10% and 30%. (ref.: [17] Automotive Thermoelectric Generators and HVAC, John Fairbanks, US Department of Energy).

8 Experiment on turbo-shaft jet engine

I will make a numerical estimation for a Seebeck thermocouple of materials that I will use in the experimental verification presented in the following chapter corresponding to the generator used in the experimental part. For numerical calculation I used formulas (5), (6) and (7) presented in Subsection 5.3. I will consider a parameter z between 0 and $5 \cdot 10^{-3} K^{-1}$, and the estimated temperature differences will be between 0 and 260^0K, potential differences to be obtained with thermocouples in which materials with operating temperatures above 2300^0C were used, and at external temperatures typical of the stratosphere. I mention these generators that operate at lower temperatures can also be used to recover the heat lost by the engine through the housings of components with lower temperatures, but suitable for energy recovery as heat.

With these data, after performing the calculations I present the values in Table 4, represented graphically in Figure 10:

z	$\eta_{t=}$	$Y_{max.=}$	
t2(cold)=	200	t1(hot)=:	2600
0.00	0	1	
1.00	0.3118	1.5492	
2.00	0.4325	1.9494	
3.00	0.5014	2.2804	
4.00	0.5474	2.5690	
5.00	0.5809	2.8284	
t2(cold)=	200	t1(hot)=:	1100
0.00	0.0000	1.0000	
1.00	0.1588	1.2845	
2.00	0.2489	1.5166	
3.00	0.3091	1.7176	
4.00	0.3531	1.8974	
5.00	0.3872	2.0616	
t2(cold)=	200	t1(hot)=:	400
0.00	0.0000	1.0000	
1.00	0.0427	1.1402	
2.00	0.0750	1.2649	
3.00	0.1007	1.3784	
4.00	0.1218	1.4832	
5.00	0.1396	1.5811	

Table 4. TEG parameters values

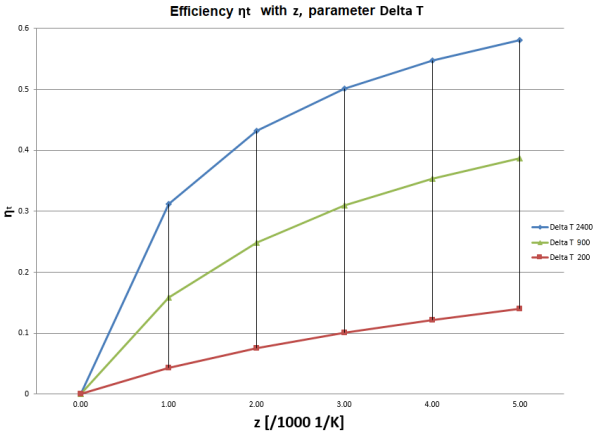

Figure 10. Efficiency η_t with z, parameter ΔT

9 Experimental Verification and Estimation of Energy Generation from Residual Heat Flown on a Turbo-Shaft Jet Engine

To estimate the power lost through the outer walls of a jet engine, I used a Titan Gas Turbine T-62T-32 turbo-shaft jet engine, manufactured by the SOLAR Division of International Harvester Company, San Diego, California, a turbo-shaft jet engine that is used for military technology (APU: Auxiliary Power Unit, for various types of military helicopters) or on ground applications, such as ground generators (GPU: Ground Power Unit, used by the US Navy and USAF). The turbo-axial jet engine on which we conducted the experiment is used to power an ultralight helicopter, according to the identification plate (Figure 13, image on the helicopter). Here are some photos of this turbo-shaft jet engine (Figures 11 and 12, obtained with the support of: "SOLAR Division of International Harvester Company, San Diego, California"):

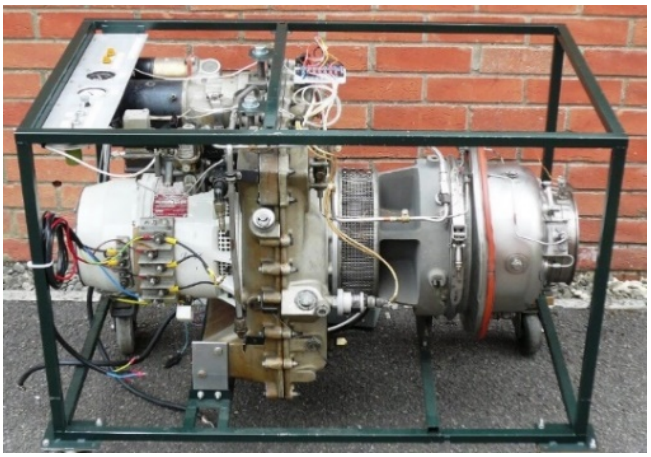

Figure 11. Turbo-shaft jet engine Solar installed on a GPU

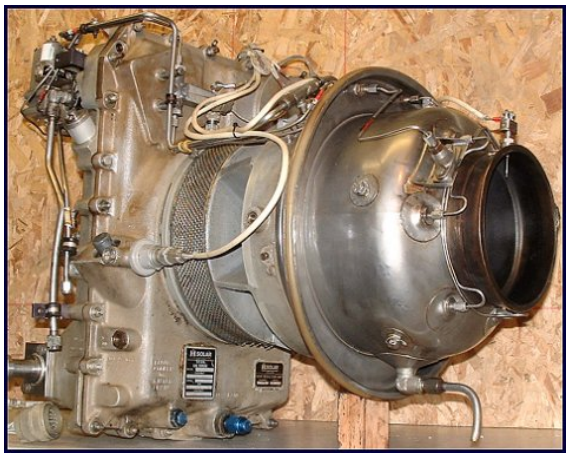

Figure 12. View of a Solar turbo-shaft jet engine

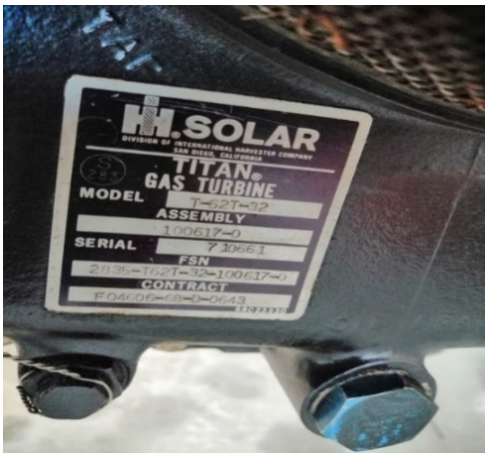

Figure 13. Identification plate of Solar turbo-shaft jet engine

Following the measurements, the temperature on the ”hot” metal part of the exhaust diffuser was 158^0C on the ”hot” side at 40% of power, and approximately 50^0C on the ”cold” side, at the same engine load. At maximum engine power, on the hot side I measured 222^0C on the ”hot” side and a temperature of approximately 50^0C on the ”cold” side. I mention that the gases in the exhaust flow have a temperature of 362^0C at a 40% power load and 567^0C at a maximum power of 100%. I also mention that the external temperature at the time of measurement was 26^0C and the atmospheric pressure at the runway level was 1011hPa. The engine's thermal load was with stabilized parameters (the helicopter at takeoff parameters).

Below I present some photos (Figures 14 and 15) that confirm the above data:

Figure 14. Hot case temperature for 100% power

Figure 15. Hot case temperature for 40% power

To estimate the power generated I will use Eureca Seebeck thermoelectric generators, manufactured by Messtechnic GmbH, type TEG2-50-50-40/200, which have a maximum power of 40W and a maximum operating temperature of 200^0C, have dimensions of 50mm x 50mm x 3.3mm thickness and a weight of 38 grames.

This is manufactured with a Bi_2Te_3-PbTe thermocouple, whose Ioffa coefficient is z=0.5·10-3K-1, according to the generator's data sheet [16], the thermoelectric potential (electric force) is 0.0516 V/K, the internal resistance is 0.673Ω, and the thermal conductivity of the plate is γ=1.90W/K.

For the experiment, I simulated the temperature of the turbo-shaft jet engine using an electrical resistance (smooth iron resistance) that I adjusted to heat up to a temperature of approximately 150^0C (so as not to destroy the Seebeck generator).

I measured the electrical parameters of the generated electrical energy that supplies a consumer (20W/6V light bulb) of 20W, slightly higher than the maximum power generated by the Seebeck generator.

According to the Eureca graph for Seebeck bridge used (courtesy: www.eureca.de) for temperature differences ΔT with values of 200^0C, 100^0C and 50^0C, graphically represented in Figure 16 shown below:

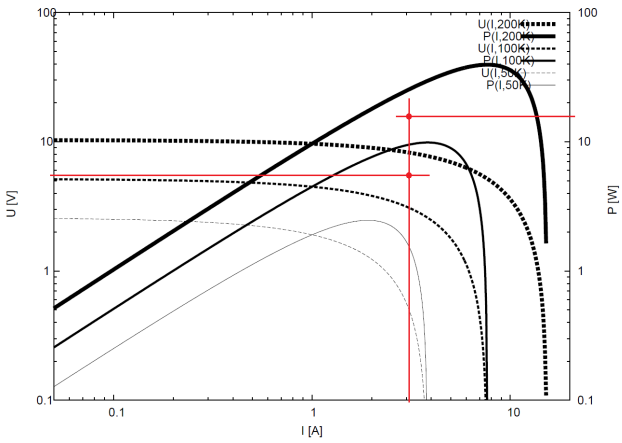

Figure 16. Equilibrium points for Eureca Seebeck bridge for Voltage and Power with Current

From Eureca data sheet in [16], the values for the Seebeck generator used are:

$\alpha = 0{,}0516$ V/K;

$\rho = 0{,}673\ \Omega$;

$\lambda = 1{,}90$ W/K.

Following the experiment carried out to simulate energy recovery from the hot zone of the turbo-shaft jet engine, the following were measured, at a temperature stabilized at 154.0^0C: U=5.33V, I=3.56A for which P=18.98W results, and after approximately 2 minutes from making contact with the electrical resistance of the Seebeck generator, the generated electric current decreased to I=3.01A for which P=16.04W and it was stabilized.

I mention when the parameters are stabilized after a decrease in the generated power of approximately 15.49%. The experiment lasted 10 minutes.

It is important to discuss the limitations of this laboratory simulation and how real-world environmental factors would affect the Seebeck generators in a practical helicopter or aircraft installation. In initial tests, attempting to mount the Seebeck modules directly onto the hot components of the turbo-shaft engine resulted in the destruction of two modules. This was caused by the lack of precise temperature control during startup and transient power settings. To prevent further damage to the COTS (Commercial Off-The-Shelf) modules, a controlled electrical resistance simulation was adopted instead. In an operational environment, high-velocity convective airflow over the engine casing would alter the boundary layers and temperature gradients, which are critical to the thermoelectric performance. Additionally, mechanical vibrations and thermal shock cycles during engine start/stop cycles could degrade the thermal contact resistance and mechanical attachment of the modules. For a production-ready aviation system, high-temperature thermoelectric materials capable of withstanding thermal shocks and uncontrolled temperature excursions must be used. Adequate mechanical fastening and thermal interface materials can mitigate contact degradation from vibration. Compared to classic gas turbines that operate under severe rotational stress and have operational lifespans of a few thousand hours, static Seebeck modules face much milder stress profiles, offering lower manufacturing and maintenance costs, with expected lifespans extending to hundreds of thousands of hours.

Below are some photos from the experiment (Figures 17, 18, 19 and 20):

Figure 17. Simulated temperature

Figure 18. TEG voltage

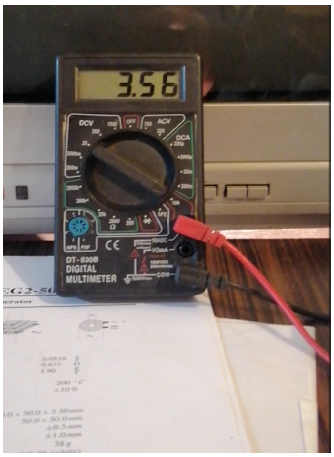

Figure 19. Initial current

Figure 20. Stabilized current

10 Conclusions and interpretation of experimental results

I have chosen this verification option because it would not have been technically possible to perform the verification on the turbo-shaft engine, first of all because the turbo-shaft is mounted on an ultralight helicopter, and at the maximum speed of the turbo-shaft engine, the Seebeck generator could be destroyed.

Thus, for a ground operating mode of the turbo-shaft engine at 40% of the maximum power, the temperature measured by me on the hot side is 158^0C, and the power is 44.0 kW.

The estimation of the power generated on a diameter of 54.293 cm (according to the technical sheet of the turbo-shaft) will be:
Perimeter: 54.293 x 3.141592 = 170.566 cm, on which 170.566: 5 = 34 pieces Seebeck plates can be mounted.
For the length of the hot side of approximately 50 cm, 340 Seebeck plates could be mounted, which will generate:
340 x 16.04 W = 5.454 kW.

This power of 5.454 kW represents 12.40% of the useful mechanical shaft power of the engine at that speed (44.0 kW). Since casing heat and exhaust represent waste thermal energy, it is more rigorous to evaluate this recovery relative to the total chemical energy input of the fuel. Assuming a typical thermal efficiency of approximately 20% for this class of turbo-shaft engine, the total chemical energy input rate of the fuel is approximately 220.0 kW (44.0 kW / 0.20). Thus, the recovered electrical power of 5.454 kW represents approximately 2.48% of the total chemical energy input of the fuel (5.454 kW / 220.0 kW). Given that approximately 80% of the fuel's energy is lost as waste heat to the cold source (exhaust gas and engine walls), this casing recovery represents a retrieval of approximately 3.1% of the total waste thermal energy. This recovered energy is a direct gain from the casing walls, which would otherwise be lost to the environment in a standard gas turbine, and can be used to recharge the on-board batteries or drive the electric compressor. I cannot recover the energy from exhaust gases which is also a lost energy because I do not have Seebeck bridges suitable for this temperature.

REFERENCES

[1] C. Berbente, N. V. Constantinescu, *Dinamica gazelor, Partea I*, Centrul de multiplicare cursuri I.P.B., București, Romania, 1985.

[2] E. Carafoli, V. N. Constantinescu, *Dinamica fluidelor incompresibile*, Editura academiei R.S.R., București, Romania, 1981.

[3] E. Carafoli, V. N. Constantinescu, *Dinamica fluidelor compresibile*, Editura academiei R.S.R., București, Romania, 1984.

[4] E. Carafoli, V. N. Constantinescu, *Dinamica fluidelor viscoase în regim laminar*, Editura academiei R.S.R., București, Romania, 1987.

[5] V. N. Constantinescu, St. Găletușe, *Mecanica fluidelor și elemente de aerodinamică*, Editura didactică și pedagogică, București, Romania, 1983.

[6] M. Marinescu, Instalaţii de ardere, culegere de probleme, Editura tehnică, București, Romania, 1985.

[7] V. Pimsner, *Mașini cu palete, procese și caracteristici*, Editura tehnică, București, Romania, 1988.

[8] V. Pimsner, *Motoare aeroreactoare*, Vol. **1**, Editura didactică și pedagogică, București, Romania, 1983.

[9] V. Pimsner, ș.a., *Procese în mașini termice cu palete, aplicaţii și probleme*, Editura tehnică, București, Romania, 1986

[10] V. Pimsner, ș.a., *Termodinamica tehnică, culegere de probleme*, Editura didactică și pedagogică, București, Romania, 1982.

[11] V. Stanciu, *Modelarea tracţiunii sistemelor de propulsie*, Editura Urania, ISBN 973-85530-0-8, București, Romania, 2001.

[12] M. Tomescu, *Proprietăţile combustibililor și lubrifianţilor pentru motoarele de aviaţie*, Editura tehnică, București, Romania, 1985.

[13] V. Stanciu, G. Cican, *Simularea performanţelor turbomotoarelor de aviaţie în FORTRAN*, Editura Printech, ISBN 978-606-23-0310-5, București, Romania, 2015.

[14] Alejandro Millán-Merino, Pierre Boivin. *A new single-step mechanism for hydrogen combustion. Combustion and Flame*, 2024, 268, pp.113641. 10.1016/j.combustflame.2024.113641. hal-04943874

[15] V. A. Kirillin, *Termodinamica*, Editura ştiinţifică și enciclopedică, București, Romania, 1985.

[16] * * * http//:www.eureca.de, Catalog.

[17] * * * Automotive Thermoelectric Generators and HVAC, John Fairbanks, US Department of Energy, 2013 Annual Merit Review and Peer Meeting DOE Vehicle Technologies Office, Washington DC, May 17, 2013.

[18] G. J. Snyder, E. S. Toberer, *Complex Thermoelectric Materials*, Nature materials, https://en.wikipedia.org/wiki/Doi_(identifier):https://doi.org/10.1038%2Fnmat2090. https://en.wikipedia.org/wiki/PMID_(identifier) https://pubmed.ncbi.nlm.nih.gov/18219332, 2008.

[19] G. S. Nolas, J. Sharp, H. J. Goldsmid, *http://link.springer.com/10.1007/978-3-662-04569-5,* Springer Series in Materials Science, Vol. **4**, Berlin, Heidelberg: Springer- Verlag Berlin Heidelberg New York. https://en.wikipedia.org/wiki/Doi_(identifier):https://doi.org/10.1007%2F978-3-662-04569-5. https://en.wikipedia.org/wiki/ISBN_(identifier) https://en.wikipedia.org/wiki/Special:BookSources/3-540-41245-X, 2001.

[20] * * * http//:www.pyromation.com, Thermocouple Material Specifications.

[21] S. Nutu, *Electro-jet engine: a jet engine without turbine - Part 1: Presentation of electro-jet engine,* INCAS BULLETIN, Vol. 17 Issue 4, October-December 2025, Bucharest, DOI: 10.13111/2066-8201.2025.17.4.10, ISSN2066-8201

[22] S. Nutu, *Electro-jet engine: a jet engine without turbine - Part 2: Electric power generation,* INCAS BULLETIN, Vol. 17 Issue 4, October-December 2025, Bucharest, DOI: 10.13111/2066-8201.2025.17.4.11, ISSN2066-8201

[23] *** NBS Monograph 40, U.S. Department of Commerce, Thermocouple Materials;

[24] *** Englehard Industries, Inc., K-76 Technical Reference, Other Types of Thermocouples;

[25] *** Barbara Hudson, JMS Southeast, Inc., Type M and K Thermocouples;

[26] *** https://tecteg.com Tellurex, Inc., TEG-Seebeck Technology;

[27] *** Jeffrey G. Snyder, Eric S. Toberer, Complex Thermoelectric Materials;

[28] *** https://www.prattwhitney.com P&W Canada RTX Corp. United Technologies.

[29] Prakash, Om & Kashyap, Ishan & Kumar, Ayush & Bhushan, Bharath & Kumar, Anil & Chauhan, Prashant. (2021). Automobile based heat energy recovery systems. WEENTECH Proceedings in Energy. 11-23. 10.32438/WPE.022021.

[30] Wang, J.; Yin, Y.; Che, C.; Cui, M. Research Progress of Thermoelectric Materials—A Review. *Energies* **2025**, *18*, 2122. https://doi.org/10.3390/en18082122

[31] G, Krupanidhi & A, Ramya & B, Sowmya. (2022). Thermoelectric Generators and the Seebeck Effect. World Journal of Advanced Research and Reviews. 16. 1448-1455. 10.30574/wjarr.2022.16.3.1409.

[32] Andrew Royale, Milan Simic, Research in Vehicles With Thermal Energy Recovery Systems, Procedia Computer Science, Volume 60, 2015, Pages 1443-1452, ISSN 1877-0509, https://doi.org/10.1016/j.procs.2015.08.221.

[33] Jin-Cheng Zheng, Recent advances on thermoelectric materials Front. Phys. China, 2008, 3(3): 269-279

[34] Clotilde Boulanger, Thermoelectric Material Electroplating: a Historical Review, Journal of ELECTRONIC MATERIALS, Vol. 39, No. 9, 2010, DOI: 10.1007/s11664-010-1079-6

[35] John Davison, Energy Consultant, Cheltenham, Glos., UK, A review of gas turbines and their ability to use hydrogen containing fuel gas, Report for Energy Technologies Institute September 2016

[36] Salehi, Vahid Douzloo, Munich University of Applied Sciences, International conference on engineering design, Application of a holistic approach of hydrogen internal combustion engine (hice) busses, 16-20 August 2021, Gothenburg, Sweden

[37] Giacomazzi, E.; Troiani, G.; Di Nardo, A.; Calchetti, G.; Cecere, D.; Messina, G.; Carpenella, S., Hydrogen Combustion: Features and Barriers to Its Exploitation in the Energy Transition. Energies 2023, 16, 7174. https://doi.org/10.3390/en16207174

0 Research Index

Author Guidelines

London Journal of Engineering Research

Journals Press | Open Access | Peer Reviewed | COPE Compliant

---

I. OUR EDITORIAL PHILOSOPHY

At Journals Press, we recognize that true scientific advancement relies on rigorous validation and unobstructed distribution. London Journal of Engineering Research serves as a premium, open-access platform committed to upholding the highest echelons of academic integrity. Our objective is to streamline the publication journey, empowering researchers to focus resolutely on their discoveries rather than administrative burdens.

II. UNRESTRICTED MANUSCRIPT SUBMISSION

We believe rigid formatting requirements stifle innovation and delay dissemination. Therefore, we invite you to submit your manuscript in its current, natural format.

- **Accepted Formats:** Microsoft Word (.docx), LaTeX (.tex), PDF (.pdf), or standard Rich Text.
- **Requirements:** Only the manuscript file, corresponding author's name, and contact email.
- **Heading Style:** Final typeset articles normally use sentence case for author-created headings, while preserving acronyms, proper nouns, gene/species names, chemical notation, brand names, Roman numerals, and approved manual capitalization.
- **Submission Portal:** https://journalspress.com/submit-manuscript/

Upon submission, our elite pre-production team manages all typesetting and template conversion, establishing a sleek, review-ready manuscript.

III. NEXT-GENERATION PEER REVIEW

Credibility is forged through meticulous evaluation. London Journal of Engineering Research deploys an innovative, multi-tiered double-blind peer review framework ensuring objective, uncompromised scrutiny.

1. **Algorithmic & Editorial Triage:** Submissions undergo AI-assisted screening for ethical compliance, originality, and scope alignment before human editorial assessment.
2. **Expert Panel Evaluation:** Manuscripts are routed to domain-specific scholars. Reviewers focus on methodological soundness, data integrity, and analytical rigor.
3. **Collaborative Refinement:** Authors receive comprehensive, line-numbered Review Reports, enabling precise, constructive dialogues. Modifications are requested natively via our intuitive Author Dashboard.

IV. THE PUBLICATION PIPELINE

We emphasize speed without compromising precision. Our publication lifecycle is entirely transparent:

1. **JournalPreview:** Following acceptance, a fully typeset galley proof is released to the authors. This version contains line numbers allowing for targeted, final typographical refinements.
2. **Online First:** Once the JournalPreview is ratified, the corrected article is officially launched online. It receives an active Digital Object Identifier (DOI), rendering it immediately citable while awaiting final issue compilation.
3. **Issue Compilation & Print Archive:** The paper is aggregated into its respective Volume and Issue. Premium, hardbound volumes are cataloged and distributed to premier academic institutions globally.

V. COMMITMENT TO OPEN SCIENCE

London Journal of Engineering Research champions the unhindered flow of information.

- **Absolute Open Access:** All publications are universally accessible from the moment of launch under the CC BY-NC-ND 4.0 license, dismantling paywalls and democratizing knowledge.
- **Immutable Archiving:** Research is redundantly decentralized across state-of-the-art global data repositories, safeguarding the scholarly record for posterity.

Connect with Journals Press

Submit Manuscript: https://journalspress.com/submit-manuscript/

Official Gateway: https://journalspress.com

Editorial Assistance: support@journalspress.com

Redefining scholarly excellence. Shaping the narrative of tomorrow.

Go green. Help protect the environment.

The journal is available in

Hardbound printed edition, interactive PDF, EPUB, XML, Markdown, JATS and Flipbook.

Online ISSN 2631-8482

journalspress.com

THIS JOURNAL SUPPORT AUGMENTED REALITY APPS AND SOFTWARES